Galaxy And Mass Assembly (GAMA): The sSFR–M$_*$ relation part I – $\sigma_{\rm sSFR}$–M$_*$ as a function of sample, SFR indicator, and environment

L. J. M. Davies ,[1]★ C. del P. Lagos ,[1,2] A. Katsianis ,[3] A. S. G. Robotham ,[1,2]
L. Cortese ,[1,2] S. P. Driver,[1] M. N. Bremer,[4] M. J. I. Brown,[5] S. Brough ,[6]
M. E. Cluver ,[7,8] M. W. Grootes,[9] B. W. Holwerda ,[10] M. Owers[11] and S. Phillipps [4]

[1]*ICRAR, The University of Western Australia, 35 Stirling Highway, Crawley, WA 6009, Australia*
[2]*ARC Centre of Excellence for All Sky Astrophysics in 3 Dimensions (ASTRO 3D)*
[3]*Department of Astronomy, Universitad de Chile, Camino El Observatorio 1515, Las Condes, 7591245 Santiago, Chile*
[4]*School of Physics, University of Bristol, Tyndall Avenue, Bristol BS8 1TL, UK*
[5]*School of Physics and Astronomy, Monash University, Clayton, VIC 3800, Australia*
[6]*School of Physics, University of New South Wales, Sydney, NSW 2052, Australia*
[7]*Centre for Astrophysics and Supercomputing, Swinburne University of Technology, John Street, Hawthorn, VIC 3122, Australia*
[8]*Department of Physics and Astronomy, University of the Western Cape, Robert Sobukwe Road, Bellville 7535, South Africa*
[9]*ESA/ESTEC SCI-S, Keplerlaan 1, NL-2201 AZ Noordwijk, the Netherlands*
[10]*Department of Physics and Astronomy, University of Louisville, 102 Natural Science Building, Louisville, KY 40292, USA*
[11]*Department of Physics and Astronomy, Macquarie University, North Ryde, NSW 2109, Australia*

ABSTRACT

Recently, a number of studies have proposed that the dispersion along the star formation rate (SFR) – stellar mass relation ($\sigma_{\rm sSFR}$–M_*) – is indicative of variations in star formation history driven by feedback processes. They found a 'U'-shaped dispersion and attribute the increased scatter at low and high stellar masses to stellar and active galactic nuclei feedback, respectively. However, measuring $\sigma_{\rm sSFR}$ and the shape of the $\sigma_{\rm sSFR}$–M_* relation is problematic and can vary dramatically depending on the sample selected, chosen separation of passive/star-forming systems, and method of deriving SFRs (i.e. Hα emission versus spectral energy distribution fitting). As such, any astrophysical conclusions drawn from measurements of $\sigma_{\rm sSFR}$ must consider these dependencies. Here, we use the Galaxy And Mass Assembly survey to explore how $\sigma_{\rm sSFR}$ varies with SFR indicator for a variety of selections for disc-like 'main-sequence' star-forming galaxies including colour, SFR, visual morphology, bulge-to-total mass ratio, Sérsic index, and mixture modelling. We find that irrespective of sample selection and/or SFR indicator, the dispersion along the sSFR–M_* relation does follow a 'U'-shaped distribution. This suggests that the shape is physical and not an artefact of sample selection or method. We then compare the $\sigma_{\rm sSFR}$–M_* relation to state-of-the-art hydrodynamical and semi-analytic models and find good agreement with our observed results. Finally, we find that for group satellites this 'U'-shaped distribution is not observed due to additional high scatter population at intermediate stellar masses.

Key words: galaxies: evolution – galaxies: general – galaxies: groups: general.

1 INTRODUCTION

Star-forming galaxies over a range of epochs and environments have been found to display a tight correlation between their star formation rate (SFR) and stellar mass (M_*), described as the star-forming sequence (SFS, or star-forming 'main sequence'; Elbaz et al. 2007; Noeske et al. 2007; Salim et al. 2007; Whitaker et al. 2012; Davies

et al. 2016). This sequence has been shown to be largely linear out to high redshift, but with increasing normalization as a function of look-back time (e.g. Lee et al. 2015; Schreiber et al. 2015). The physical interpretation of these observations (i.e. Bouché et al. 2010; Daddi et al. 2010; Genzel et al. 2010; Lagos et al. 2011; Davé et al. 2013; Lilly et al. 2013; Mitchell et al. 2016) is that the bulk of star-forming galaxies reside in a self-regulated equilibrium state, where the inflow rate of gas for future star formation is balanced by the rate at which new stars are formed and the outflow of gas from feedback events [i.e. supernovae (SNe) and active galactic nuclei (AGN)].

★ E-mail: luke.j.davies@uwa.edu.au

However, within the full sSFR–M_* plane the situation is more complex. While this simple self-regulated model is likely to fit for sources that sit close to the locus of the SFS, there exist various other population that deviate from this model, such as the passive cloud that sits below the SFS, 'green valley' sources that sit between the SFS and passive cloud, and star-bursting sources that reside above the SFS. More recent results have found that galaxies move significantly within the SFS over their lifetime based on small star-burst/quenching events (i.e. Magdis et al. 2012; Tacchella et al. 2016), such that the locus of the SFS remains constant at a given epoch, but with individual galaxies move within the SFS producing the observed scatter. In addition, there has been recent evidence to suggest that the SFS is non-linear in the high stellar mass regime and flattens (e.g. Rodighiero et al. 2010; Elbaz et al. 2011; Whitaker et al. 2012; Lee et al. 2015; Katsianis, Tescari & Wyithe 2016; Grootes et al. 2017, 2018). This is likely to be caused by the inclusion of non-star-forming bulge components in stellar mass estimates at $\log_{10}[M_*/M_\odot] > 10$ (Erfanianfar et al. 2016). The flattening is found to be removed when only considering disc-dominated systems (e.g. Abramson et al. 2014; Willett et al. 2015) and/or just the disc components of galaxies (Davies et al., in preparation – paper II in this series – and Cook et al., in preparation).

The position of a galaxy within the sSFR–M_* plane is largely determined by its star formation history (SFH, Madau, Pozzetti & Dickinson 1998; Kauffmann et al. 2003). This history is governed by many events, which occur in the lifetime of the galaxy that can fundamentally affect its trajectory through the sSFR–M_* plane, such as gas accretion (Kauffmann et al. 2006; Sancisi et al. 2008; Mitchell et al. 2016), mergers (e.g. Bundy et al. 2004; Baugh 2006; Kartaltepe et al. 2007; Bundy et al. 2009; de Ravel et al. 2009; Jogee et al. 2009; Lotz et al. 2011; Robotham et al. 2014, and see review of Conselice 2014), SNe feedback (Dekel & Silk 1986; Dalla Vecchia & Schaye 2008; Scannapieco et al. 2008), and AGN feedback (Kauffmann et al. 2004; Fabian 2012), environmental effects such as starvation, strangulation, and stripping (e.g. Giovanelli & Haynes 1985; Moore et al. 1999; Peng et al. 2010; Cortese et al. 2011; Darvish et al. 2016), and morphological changes (Conselice 2014; Eales et al. 2015). It is the combination of these SFHs that ultimately result in the distribution of points in the sSFR–M_* plane (Abramson et al. 2016). As such, understanding the global distribution of sources within this plane, the position of various sub-population split on properties such as environment, morphology and structure, and physical mechanisms that result in galaxies moving through the plane is essential to our parametrization of the factors driving galaxy evolution.

One key diagnostic of these physical mechanisms is the dispersion along the sSFR–M_* relation ($\sigma_{\rm sSFR}$–M_*, Guo et al. 2015; Willett et al. 2015; Katsianis et al., in preparation). This dispersion is essentially a metric of the variation in a galaxy's recent SFH at a given stellar mass. For example, recent quenching and star-burst events push galaxies below and above the SFS, respectively, increasing the dispersion. In addition, as these events have opposite effects in terms of sSFR, asymmetry in the distribution of points about the SFS at a given mass is indicative of predominant quenching/starbursts

There is currently rich debate as to the shape of the $\sigma_{\rm sSFR}$–M_* relation. At high redshifts ($z > 1$) and for predominantly UV-derived SFRs, authors have generally found a relatively constant dispersion of ~0.3 dex (Elbaz et al. 2007; Noeske et al. 2007; Rodighiero et al. 2010; Whitaker et al. 2012; Schreiber et al. 2015). However, other authors have suggested that this dispersion may increase with decreasing stellar mass at $\log_{10}[M_*/M_\odot] < 10$ in high-redshift samples and be driven by stochastic SFHs in low-

mass galaxies (Santini et al. 2017). For more nearby samples and higher stellar mass galaxies, other studies have identified a dispersion that increases at $\log_{10}[M_*/M_\odot] > 10$ (Guo et al. 2015) and attribute the large dispersion to the presence of bulges and bars (their sample is purely selected based on sSFR and thus contain bulge + disc systems). To overcome this, Willett et al. (2015) explore the $\sigma_{\rm sSFR}$–M_* relation in a morphologically selected sample of disc-like spirals from Galaxy Zoo (Willett et al. 2013). They find a minimum vertex parabolic ('U'-shaped) dispersion that decreases with stellar mass from $\log_{10}[M_*/M_\odot] \sim 8$–10 and then increases at $\log_{10}[M_*/M_\odot] \sim 10$–11.5. This is loosely consistent with the Guo et al. (2015) results at the high-mass end, but finds the upturn in dispersion occurs at higher masses. In addition, there also appears to be some variation in the literature measurements of $\sigma_{\rm sSFR}$–M_* depending on the SFR indicator used; with UV-, Hα-, and SED-derived SFRs producing different dispersions. This is potentially due to the varying biases included in different SFR indicators and the physical time-scales over which they probe; for example Hα-derived SFRs are much more sensitive to short time-scale fluctuations in SFH (for a detailed discussion of SFR indicators, their biases, and time-scales see Kennicutt & Evans 2012; Davies et al. 2015b, 2016, and Katsianis et al. 2017 for a simulations perspective).

Evidently the observational picture is far from clear, with different teams applying different selection methods and using different SFR indicators finding different results. However, hydrodynamical simulations can offer some further insights into the $\sigma_{\rm sSFR}$–M_* relation and the physical processes driving its shape. Sparre et al. (2015) use the Illustris simulation (Vogelsberger et al. 2014) to explore the evolution of the sSFR–M_* relation for all Illustris galaxies and at $z \sim 0$ find a relatively flat $\sigma_{\rm sSFR}$–M_* at $9 < \log_{10}[M_*/M_\odot] < 10.5$ and increasing dispersion to higher masses. However, they do not make any selection to exclude passive systems, and hence this increased dispersion is likely due to the passive population becoming more prevalent at high stellar masses.

More recently, Katsianis et al. (in preparation) applied a similar approach to the EAGLE simulation (Crain et al. 2015; Schaye et al. 2015; McAlpine et al. 2016; Matthee & Schaye 2018) and find a minimum vertex parabolic ('U'-shaped) $\sigma_{\rm sSFR}$–M_* relation similar to that of Willett et al. (2015) – note that Matthee & Schaye (2018) find a linearly decreasing $\sigma_{\rm sSFR}$–M_* when excluding the passive population based on sSFR (which we also explore here). Moreover, the work of Katsianis et al. (in preparation) also allows an exploration of the physical mechanisms that are driving this dispersion. First, they rerun their analysis with no-AGN feedback and find that the dispersion is dramatically reduced at the high stellar mass end, suggesting it is AGN feedback that drives the high dispersion at $\log_{10}[M_*/M_\odot] \sim 10$–11.5 observed by Guo et al. (2015) and Willett et al. (2015) – this is also discussed in Matthee & Schaye (2018). Next, they rerun their analysis with stellar feedback turned off and find a reduced scatter at the low stellar mass end, suggesting it is stellar feedback/star formation that drives the observed dispersion at these lower masses.

Similarly, using the semi-analytic model (SAM), Shark, Lagos et al. (2018) showed that the adopted star formation law had a strong effect on the scatter of the SFS (through their effect on the time-scales of atomic to molecular hydrogen and molecular-to-stars conversion). However, the choice of star formation law rarely affected the zero-point of the main sequence. These simulation results suggest that the scatter of the SFS is rich in information about the physics of galaxy formation and provide us with both a prediction for the shape of the $\sigma_{\rm sSFR}$–M_* relation and the physical

mechanisms driving it. We must now aim to test this prediction via our observational samples.

In this series of papers, we produce a detailed analysis of the sSFR–M_* plane and the factors driving its formation. In this first paper, we explore the observed dispersion along the SFS and its variation with sample selection, SFR indicator, and group/isolated environment using the Galaxy And Mass Assembly (GAMA) sample. We explore whether the variation in the $z \sim 0$ σ_{sSFR}–M_* observed by previous authors is physical or an artefact of their chosen method. Following this, we will determine how the sSFR–M_* plane can be sub-divided into different population based on various morphological and structural tracers, how this varies with environment, and how these population are indicative of different evolutionary pathways through the sSFR–M_* plane. Finally, we will use our new SED fitting code PROSPECT (Robotham et al., in preparation) to determine SFHs and AGN fractions for galaxies across the sSFR–M_* plane and explore the physical mechanisms that have shaped the $z \sim 0$ SFR–M_* relation using all observations presented in the series.

This paper is organized as follows. In Section 2, we discuss the observational samples used in this work and briefly describe our choice of SFR indicators. In Section 3, we detail different methods for selecting the SFS based on SFR, colour, and morphology/structure. In Section 4, we present the resultant σ_{sSFR}–M_* relation derived from each sample and explore its variation with SFR indicator and environment. We also compare our results to the Shark and EA-GLE simulations. Finally, in Section 5 we present our conclusions. Throughout this paper, we use a standard ΛCDM cosmology with $H_0 = 70 \, \mathrm{km \, s^{-1} \, Mpc^{-1}}$, $\Omega_\Lambda = 0.7$, and $\Omega_M = 0.3$.

2 DATA AND SAMPLE SELECTIONS

2.1 Galaxy And Mass Assembly Survey

The GAMA survey covers $286 \, \mathrm{deg}^2$ to a main survey limit of $r_{AB} < 19.8 \, \mathrm{mag}$ in three equatorial (G09, G12, and G15) and two southern (G02 and G23 survey limit of $i_{AB} < 19.2 \, \mathrm{mag}$ in G23) regions. The limiting magnitude of GAMA was initially designed to probe all aspects of cosmic structures on 1 kpc to 1 Mpc scales spanning all environments and out to a redshift limit of $z \sim 0.4$. The spectroscopic survey was undertaken using the AAOmega fibre-fed spectrograph (Saunders et al. 2004; Sharp et al. 2006) in conjunction with the two-degree field (Lewis et al. 2002) positioner on the Anglo–Australian telescope and obtained redshifts for ~240 000 targets covering $0 < z \lesssim 0.5$ with a median redshift of $z \sim 0.25$, and highly uniform spatial completeness (see Baldry et al. 2010; Robotham et al. 2010; Driver et al. 2011; Hopkins et al. 2013, for summary of GAMA observations).

Full details of the GAMA survey can be found in Driver et al. (2011, 2016a), Liske et al. (2015), and Baldry et al. (2018). In this work, we utilize the data obtained in the three equatorial regions, which we refer to here as GAMA $\mathrm{II_{Eq}}$. Stellar masses for the GAMA $\mathrm{II_{Eq}}$ sample, and those used in this work, are derived from the *ugriZYJHK* photometry using a method similar to that outlined in Taylor et al. (2011) – assuming a Chabrier initial mass function (IMF; Chabrier 2003), GAMA DMU StellarMassesLambdarV20. All photometry used in this work is measured using the Lambda Adaptive Multi-Band Deblending Algorithm for R and presented in Wright et al. (2016), GAMA DMU LambdarPhotometryV01.

In this paper, we also use the recent GalaxyZoo classifications that are based on the Kilo Degree Survey (KiDS, de Jong et al. 2013, 2015, 2017) imaging in the GAMA regions. For these classifications, 49 851 galaxies were selected from the GAMA equatorial
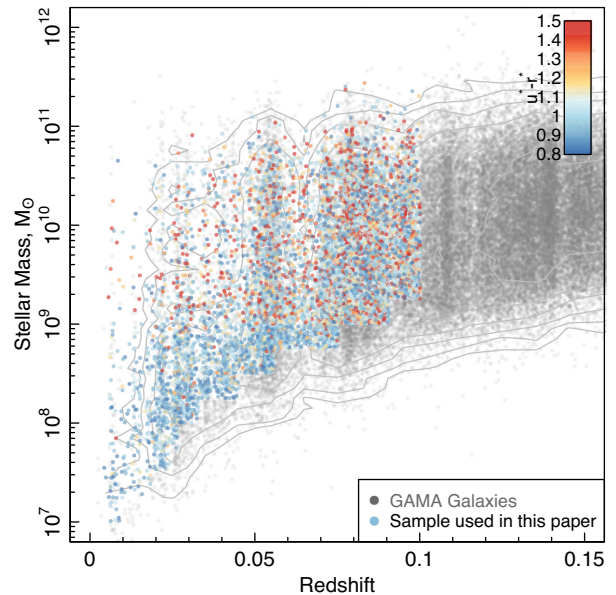

Figure 1. The redshift–stellar mass distribution of galaxies used in this work in comparison to the full GAMA sample. We initially select isolated (non-group or pair) galaxies in volume-limited samples in $\log_{10}[M_*/\mathrm{M}_\odot] = 0.25$ bins of stellar mass (see Section 2.1 for details). Selected points are coloured by their rest-frame, extinction-corrected $u - r$ colour. The contours display the density of GAMA points.

fields with redshifts $z < 0.15$. Within GalaxyZoo, the GAMA sample received almost two million classifications from over 20 000 unique users in 12 months. The GAMA–KiDS GalaxyZoo classifications use the standard decision tree implemented for current GalaxyZoo projects. A full description of the GAMA–KiDS GalaxyZoo effort can be found in Kelvin et al. (in preparation).

In this work, we further restrict our sample to galaxies within rolling volume-limited samples and initially galaxies that are not in either a group or pair in the GAMA group catalogues of Robotham et al. (2011), i.e. isolated centrals, GAMA DMU GroupFindingV10. To define our volume-limited samples, we follow a similar approach to Lange et al. (2016) and split the full GAMA catalogue into $\Delta\log_{10}[M_*/\mathrm{M}_\odot] = 0.25$ bins of stellar mass. For each bin, we calculate the redshift where 97.7 per cent of the sample has a maximum observable redshift ($V_{\max}$) greater than the median $V_{\max}$ of the bin. We then exclude all galaxies above this redshift, within the particular stellar mass bin. Finally, we put an upper redshift limit of $z < 0.1$. This process allows us to extend to lower stellar masses in our very local sample.

The resultant redshift–stellar mass selection of our sample in comparison to the full GAMA sample is shown in Fig. 1. The $z < 0.1$ restriction is to largely remove any evolution in the SFS across our sample redshift range. In addition, a number of GAMA data products that are required for our analysis are only available for $z < 0.1$ GAMA galaxies (see Section 3). The isolated centrals restriction allows us to remove any additional environmental quenching effects that may induce additional scatter in the SFS, which is not driven by feedback (however, c.f. Barsanti et al. 2018, find that groups can affect galaxies SF properties out to large radii). Note that we do not include group centrals in our sample as there is currently some debate as to whether or not these galaxies undergo environmental quenching (e.g. see Wang et al. 2018). However, we do perform our analysis including group centrals and find that it does not signifi-

cantly affect our results. The effect of group environment on σ_{sSFR} is then explored further in Section 4.3 and in the following papers in this series. In total, there are 9005 galaxies in our starting sample.

2.1.1 *GAMA SFR indicators*

The GAMA SFR indicators used in this work are described at length in Davies et al. (2016). Briefly, we use (i) MAGPHYS-derived SFRs outlined in Driver et al. (2018) and based on the energy balance SED-fitting code MAGPHYS (da Cunha, Charlot & Elbaz 2008), (ii) combined Ultraviolet and Total Infrared (UV + TIR) SFRs derived from the Brown et al. (2014) galaxy spectra, (iii) Hα-derived SFRs using GAMA spectra discussed in Liske et al. (2015) and the process outlined in Gunawardhana et al. (2011, 2015) and Hopkins et al. (2013), and using the line measurements of Gordon et al. (2017), (iv) *Wide-field Infrared Survey Explorer* (*WISE*) W3-band SFRs derived using the prescription outlined in Cluver et al. (2017), and (v) extinction-corrected *u*-band SFRs derived using the GAMA rest-frame *u*-band luminosity and $u - g$ colours from Davies et al. (2016). All SFRs are scaled to a Chabrier IMF and for further details of these SFR indicators and their derivation see Davies et al. (2016).

We repeat all of the analysis in this paper for each of these SFR indicators, but for clarity we initially only show results for MAGPHYS-derived SFRs. Similar figures for all of our indicators are presented in the Appendix and discussed in Section 4. We note here that different SFR indicators can be appropriate for different science cases, and contain different biases/assumptions, as such we consider a variety here.

3 ISOLATING THE TARGET POPULATION

In order to explore the stellar mass dependence on σ_{sSFR}, and in a similar manner to previous authors, we must first isolate our population of interest. The method by which this is undertaken is largely dependent on the specific scientific question being addressed (i.e. see Renzini & Peng 2015). For example, if we wished to study the dispersion within the SFS to explore self-regulated growth via star formation, we may select sources based solely on SFR to exclude passive systems. Conversely, if we wish to investigate the SFH of star-forming discs we may wish to isolate morphologically selected disc-like systems, irrespective of their position in the sSFR–M_* plane. However, care must then be taken when drawing inferences regarding the σ_{sSFR}–M_* relation when applying different selection methods, as these can significantly affect the observed distribution. For example, is the parabolic distribution observed by previous authors largely driven by sample selection and not pure physical processes?

Here, we aim to explore the impact of sample selection on the σ_{sSFR}–M_* relation and thus provide a robust description of the intrinsic shape of the dispersion. In the following sub-sections, we explore a number of different selection criteria for identifying sources that may be used to parametrize σ_{sSFR}–M_*. In subsequent sections, the impact of each of these selections on the shape of the derived σ_{sSFR} relation will be explored. The population selected by each of these selections is displayed in Fig. 2 for MAGPHYS-derived sSFRs. In Section 4.0.1, we will also explore using a non-physically motivated mixture-modelling method to determine the σ_{sSFR}–M_*, but separate it from the physically motivated selection applied here.

3.1 No selection

First, we explore the σ_{sSFR}–M_* relation with no selection applied to the population (other than those previously described). This sam-

ple contains all 9005 sources with both star-forming and passive systems, and morphological pure discs, ellipticals, and two component disc + bulge systems. The σ_{sSFR}–M_* relation derived from this distribution is most directly comparable to the previous simulation results from Illustris and EAGLE that do not apply any selection criteria largely because all other selections are non-trivial to compute using the simulation data. In addition, this selection is informative in its own right as it essentially describes global SFH of all galaxies at a given stellar mass and can be used to identify star-burst/quenched population irrespective of their non-star-forming properties. Panel A of Fig. 2 displays our sample with no further selection for MAGPHYS-derived SFRs (and in the appendix for all other SFR indicators).

3.2 $u - r$ colour selection

One potential method for identifying late-type (star-forming) galaxies is through rest-frame, extinction-corrected broad-band optical colours. Galaxy colours have a long history in selecting star-forming, passive, and green-valley systems (for some examples see Salim et al. 2005; Schawinski et al. 2014; Taylor et al. 2015). Old stellar population show a red colour with substantially more flux at longer wavelengths. However, with star formation activity high-mass, blue stars increasingly contribute to the galaxy's spectral shape, flattening the SED, and producing bluer colours. As such, optical colour provides a measure of recent SFH and can be used to isolate star-forming systems. Here, we use $u - r$ colour to isolate late-type, star-forming galaxies as the *u* band is strongly correlated with recent star formation (see Davies et al. 2016) and the *r* band is representative of the underlying older stellar population.

We use the GAMA extinction-corrected rest-frame $u* - r*$ colours taken from Taylor et al. (2011) and separate the population following the approach outlined in Bremer et al. (2018), where we apply a mass-dependent colour selection for star-forming galaxies of

$$u^* - r^* < 0.15 \times \log_{10}[M_*/M_\odot] + 0.05. \tag{1}$$

This relation sits between the blue and red galaxy selection lines of Bremer et al. (2018). This forms our $u - r$ colour-selected sample and is displayed in panel B of Fig. 2. 8338 star-forming sources are selected using this criteria, while 667 are classed as passive. We note that a $u - r$ colour selection is not as extreme as a pure sSFR cut (described in the next section) as the $u - r$ colour essentially probes the contribution of young stellar population over a relatively large evolutionary baseline, while sSFR measures the recently formed stellar population on a short time-scale. In addition, the $u - r$ colour selection is sensitive to dust obscuration. While we use extinction-corrected colours, these my suffer from large uncertainties in extremely dusty galaxies.

3.3 sSFR selection

It is also possible to isolate the SFS using star formation alone. To do this, one must somewhat arbitrarily choose at which SFR to divide the two population, which can have a strong effect on the measured dispersion (i.e. too low a cut and you include the passive population, too high a cut and you artificially reduce σ_{sSFR}). In addition, applying a single sSFR cut to isolate the star-forming population is only appropriate if the slope of the sSFR–M_* relation is unity, this is not the case (see panel C of Fig. 2). However, given that this approach is applied by many previous studies (i.e. Guo et al. 2015), we replicate a similar selection here. With the caveats of potential errors due to choice of star-forming-passive cut
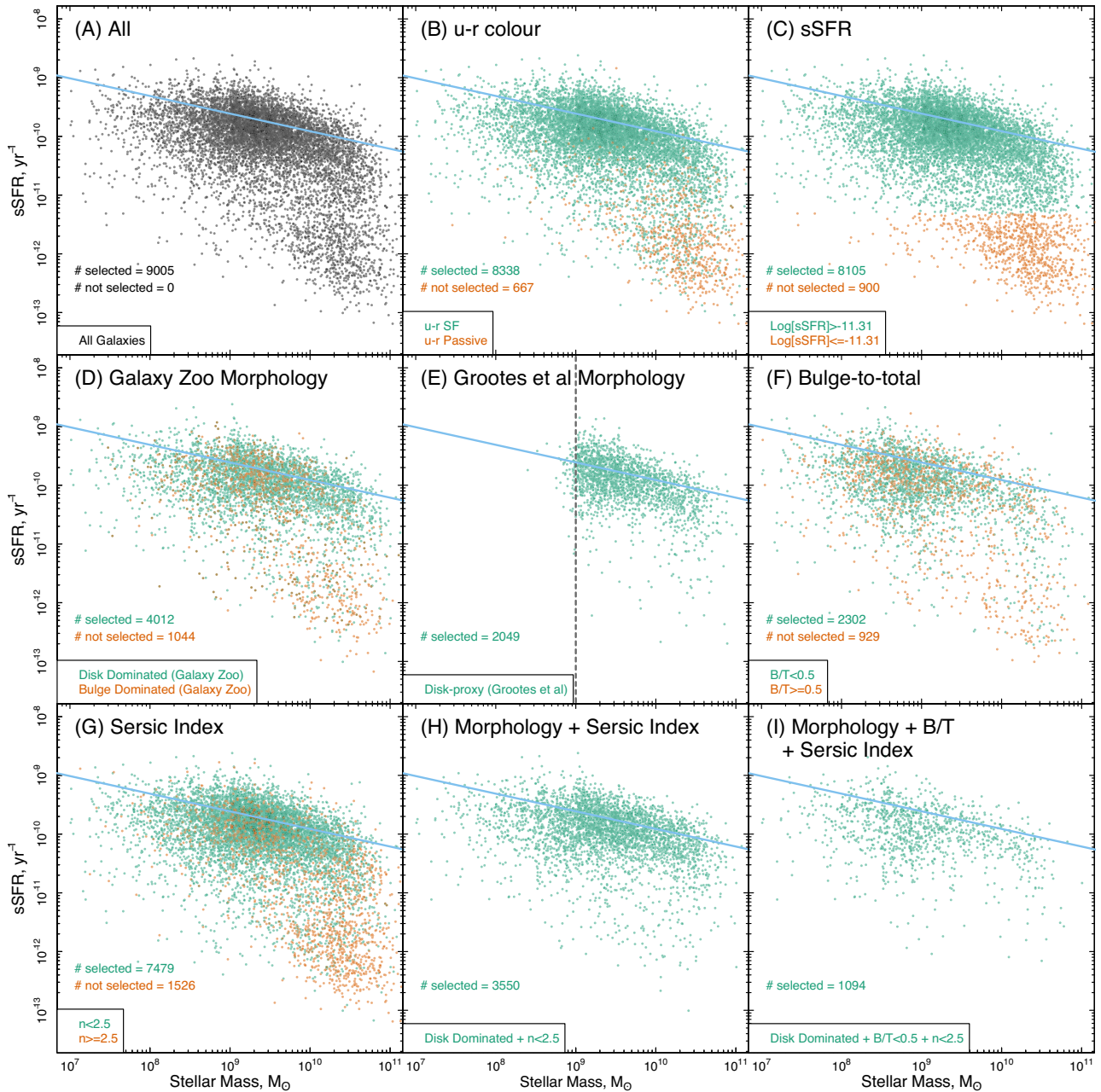
Figure 2. The sSFR$_{\text{MAGPHYS}}$–M$_*$ relation colour-coded by various selection methods for identifying the SFS. The linear fit (light blue line) is taken from Davies et al. (2016). (A): the full distribution of $z < 0.1$ GAMA galaxies that are not in a group or pair (i.e. isolated down to GAMA limit), (B): selection based on $u - r$ colour, (C): selection based on sSFR, (D): selection based on visual morphological classification from Galaxy Zoo, (E): selection based on the morphological proxy analysis of Grootes et al. (2014) – vertical dashed line shows stellar mass limit of this analysis, (F): selection based on r-band bulge-to-total light ratio (B/T) – note this sample only extends to $z < 0.06$, (G): selection based on Sérsic index, (H): selection based on visual morphology and Sérsic index selection combined, (I) selection based on visual morphology, Sérsic index, and B/T selections combined. The number of galaxies in each selection are displayed in the bottom left corner of each panel. The total number of selected and non-selected galaxies displays the number of sources for which we have the required measurements for the selection. For panels that do not have a value for 'non-selected', either the catalogue used only contains the selected sample (panel E), or the selection if knowingly incomplete and the 'non-selected' number is not informative (panels H and I).

in mind, here we isolate the SFS by selecting galaxies for which $\log_{10}[\text{sSFR, yr}^{-1}] > \text{SFS}_{10}$-ScSFR dex. Where SFS is the fit to sSFR–M$_*$ taken from Davies et al. (2016) – shown as the blue line in Fig. 2, SFS$_{10}$ is the normalization of the fit at $\log_{10}[M_*/\text{M}_\odot] = 10$ and ScSFR $= 1.4, 0.8, 0.8, 0.9$, and 0.6 for MAGPHYS, UV + TIR,

Hα, W3, and u-band SFRs, respectively (to account for varying scatter/normalization on the relations). The impact of this selection for MAGPHYS is displayed in panel C of Fig. 2. For MAGPHYS SFRs, 8105 star-forming sources are selected, while 900 are classed as passive.

3.4 Morphological/structural selections

In order to produce samples that may be used to explore the recent SFH of spiral/disc-like systems, we also use a number of different morphological selections. These selections are aimed at identifying disc-dominated systems irrespective of their position relative to the locus of the SFS, and in practice may be used to explore the evolution of all disc-like galaxies in the SFR–M_* plane.

3.4.1 Galaxy Zoo

Our initial disc-like selection is based on the GAMA–KiDS Galaxy Zoo classifications outlined in Section 2.1. For disc-dominated systems, we select galaxies that are not edge-on (so that visual classifications are not confused) and have no bulge, or are classified as a spiral:

$$(p_{no-bulge} > 0.619 \ \& \ p_{not-edge-on} > 0.715) \ | \ p_{spiral} > 0.619, \quad (2)$$

where p is the debiased vote fraction. For comparison in panel D of Fig. 2, we also show bulge-dominated systems selected as

$$p_{bulge-dominant} > 0.619 \ \& \ p_{not-edge-on} > 0.715. \quad (3)$$

This selection is based around those used by the Galaxy Zoo team in Willett et al. (2015) for spiral galaxies. Note that we do explore various other p values for each of the selections above and find that within sensible ranges it does not have a strong impact on the shape of the derived σ_{sSFR}–M_* relation. Using these selections, 4012 galaxies are classed as disc-dominated and 1044 as bulge-dominated. The remaining 3949 are two-component or ambiguous, and are excluded.

3.4.2 Grootes et al. disc proxy

Grootes et al. (2014) used a non-parametric cell-based method to identify a highly complete and pure sample of spiral galaxies at $\log_{10}[M_*/M_\odot] > 9.0$. In this approach, colour, Sérsic index, stellar mass surface density, and effective radius from SDSS imaging were used as a proxy for morphological classifications. These were then compared to previous SDSS-based Galaxy Zoo classifications to highlight the robustness of their method. Here, we use the Grootes et al. sample as spiral systems, which reside on the SFS. However, we highlight that these morphological proxies only extend down to $\log_{10}[M_*/M_\odot] \sim 9.0$ and therefore do not cover our full sample (see panel E of Fig. 2). There are 2049 source in the Grootes et al. catalogue that meet our initial selections.

3.4.3 Bulge-to-total mass

In addition to morphological selections, we can also select samples based on a galaxy's structural components. These components represent a largely non-subjective measure of structural evolution from pure disc-like systems, to two component bulge+disc, and pure spheroid ellipticals. A simple metric for these classifications is the galaxy's bulge-to-total flux ratio (B/T); the ratio of light arising from the bulge compared to total bulge + disc, where B/T = 1 is a pure elliptical and B/T = 0 is a pure disc. Using the 2-component Sérsic fits to GAMA galaxies based on SDSS *r*-band imaging (Lange et al. 2016), we select a population with B/T < 0.5 as disc-dominated systems (see panel F of Fig. 2). The analysis of Lange et al. (2016) only provides 2-component Sérsic fits at $z < 0.06$ leaving a starting sample of 3231 galaxies, 2302 of which have B/T < 0.5 and 929 B/T >

= 0.5. Thus, this selection is limited to local galaxies. Note that we repeat our analysis with a more extreme B/T < 0.3 selection to exclude equally weighted bulge-disc systems, but find similar results.

3.4.4 Sérsic index

A cruder metric for galaxy structure is the single component Sérsic index (*n*). Briefly, the Sérsic index is a measure of the shape of a galaxy's light profile, with $n = 1$ following an exponential profile, which is found to fit galaxy discs, and $n = 4$ a de Vaucouleurs profile commonly associated with spheroidal components, such as bulges and elliptical galaxies. This is simply an empirical formalism that is found to fit the 2D light profile of a galaxy but does not fully represent the 3D distribution of stars. Kelvin et al. (2012) produced single-Sérsic fits for GAMA galaxies using the SDSS and UKIDSS LAS imaging bands outlined in Hill et al. (2011). Here, we use the SDSS *r*-band Sérsic index to isolate a disc-like sample with an $n < 2.5$ selection. This selection is found to separate disc-dominated and spheroid-dominated systems in Lange et al. (2015). Panel G of Fig. 2 displays our Sérsic index selected sample isolating the SFS and removing galaxies in the passive cloud. 7478 sources are selected as low Sérsic index using this criteria, while 1526 are classed as having high Sérsic index.

3.4.5 Combined morphological selections

In addition to our individual morphological selections, we also produce samples using combined Galaxy Zoo morphology and single Sérsic Index (Panel H of Fig. 2, selecting 3550 sources) and Galaxy Zoo morphology, single Sérsic Index and B/T (Panel I of Fig. 2, selecting 1094). These samples are less complete, but form a more robust selection of disc-like systems than the individual morphological selections as they must meet two or more of our selection criteria. We do not show the 'not selected' galaxies here, as the selection is incomplete and therefore the 'not selected' population is not informative.

4 A MASS DEPENDENT σ_{sSFR}?

Using each of the sample selection methods described above, we explore σ_{sSFR} as a function of stellar mass. Here, we define σ_{sSFR} as the standard deviation of $\log_{10}[sSFR]$ for the selected population at a given stellar mass. Note that following this we also calculate the dispersion based on the interquartile range of $\log_{10}[sSFR]$, to remove any dependencies on assumption of a Gaussian-like distribution.

We take all of our selected galaxies (black points in Fig. 2A, and green points in Fig. 2B-I) and split our samples into $\log_{10}[M_*/M_\odot] = 0.5$ bins of stellar mass. Fig. 3 displays an example of the distribution of galaxies away from the median in each bin with Poisson errors, for both MAGPHYS and Hα SFRs. For this figure, we only show sources identified as disc like from our combined Galaxy Zoo morphology and Sérsic index selection (i.e. the population in Panel H of Fig. 2). This shows the spread of sSFRs away from the locus of the SFS at a given stellar mass.

For illustrative purposes only, in Fig. 3 we fit a lognormal in each mass bin (dashed lines) to highlight any deviation in the population from a symmetric lognormal distribution. Unsurprisingly, at all masses we see an asymmetric tail extending to low sSFRs indicative of a green-valley/passive population (also see Oemler et al. 2017). We also potentially see an additional star-burst population
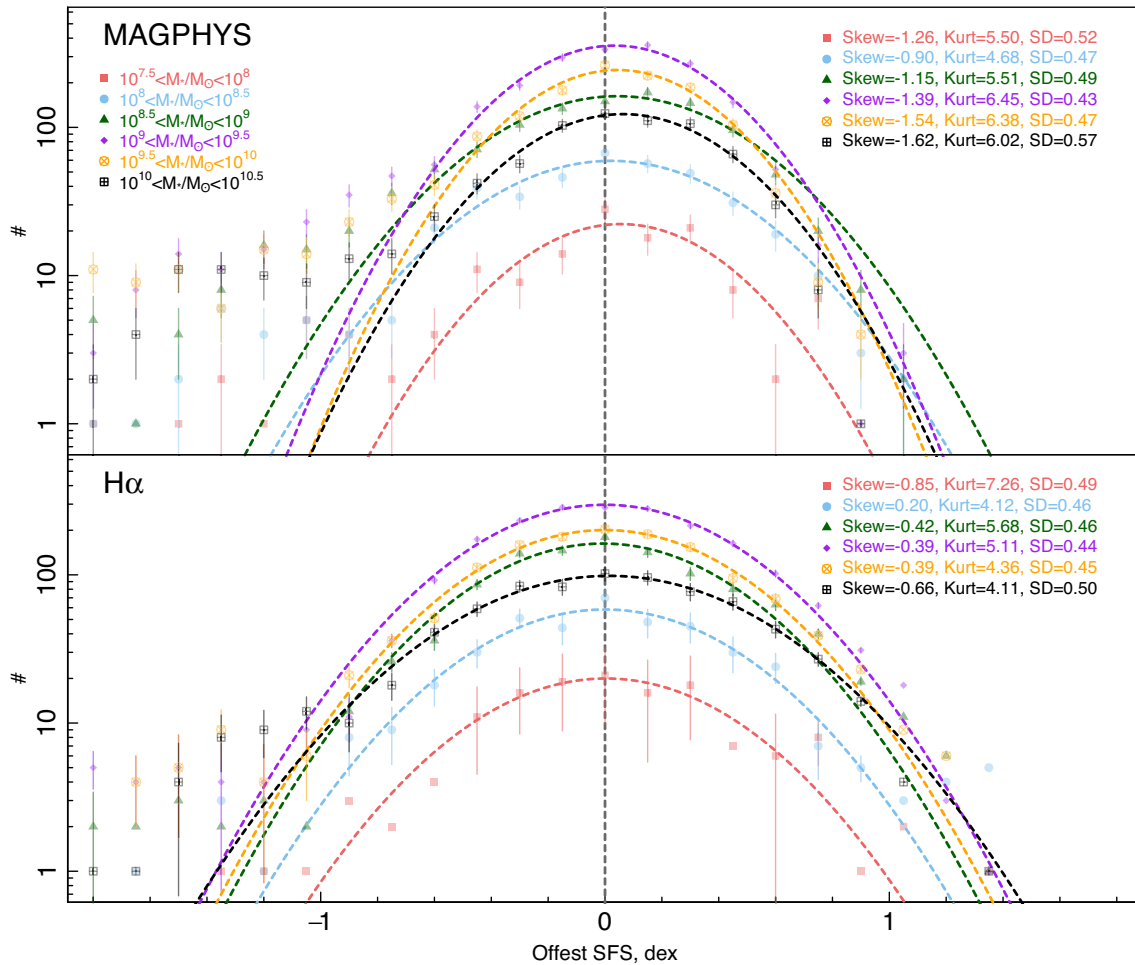
Figure 3. The distribution of points away from the SFS isolated using the combined morphology + Sérsic index selection from Section 3.4. We display the distribution in stellar mass bins for both MAGPHYS and Hα derived SFRs. Points are fit with a lognormal distribution (dashed lines) to highlight any deviation from this symmetric shape. In both SFRs and at all masses, the distributions display a negative skew value, highlighting that the distributions have asymmetric tails extending to low stellar masses. For both SFRs in all but the lowest stellar mass bin, the skew value becomes more negative to higher stellar masses suggesting that the distribution becomes more asymmetric as a function of mass.

in the Hα distribution at high SFRs (particularly seen in the positive kurtosis of the $8 < \log_{10}[M_*/M_\odot] < 9$ bin). This is interesting as it may provide evidence of short duration star-burst activity; as Hα probes star formation integrated over shorter time-scales than MAGPHYS (see Davies et al. 2015b). This will be explored further in later papers of this series.

To determine how these distributions vary as a function of stellar mass, we calculate the skewness, kurtosis, and standard deviation of $\log_{10}$[sSFRs] in each mass bin; given in the legend of Fig. 3. Interestingly, with the exception of the $8.0 < \log_{10}[M_*/M_\odot] < 8.5$ bin in Hα, all distributions show a negative skew (from the green valley/passive population) but with skewness increasing for higher stellar masses for bins at $\log_{10}[M_*/M_\odot] > 8.0$. Tentatively, this may indicate that any physical processes that drive the shape of this distribution are more likely to produce more symmetrical scatter at the low-mass end (potentially stochastic star formation bursts leading to stellar feedback), and asymmetrical scatter at the high-mass end (potentially AGN feedback). However, care must be taken as we may simply be missing a significant fraction of the quenched population at low stellar masses, and artificially removing the asymmetric tail due to selection affects imposed by GAMA. In order to go further,

we require much deeper spectroscopic surveys of the local Universe, such as the Wide Area VISTA Extragalactic Survey (WAVES Driver et al. 2016b), which will allow a detailed exploration of the distribution of star formation in very low-mass galaxies.

Taking this further, we then use the standard deviation measurements described above to derive the σ_{sSFR}–M$_*$ and measure the interquartile range in the same stellar mass bins; for all selections described in Section 3.

Fig. 4 displays σ_{sSFR} (filled circles) and the interquartile range (open squares) in $\log_{10}[M_*/M_\odot] = 0.5$ bins of stellar mass following the same panel layout as Fig. 2. Here, we only show figures for MAGPHYS SFRs, but similar figures for other SFR indicators are given in the Appendix. Statistical errors on σ_{sSFR} are calculated as

$$\text{Err}_{\sigma_{sSFR_i}} \sim \frac{\sqrt{2\sigma_{sSFR_i}^4 (N_i - 1)^{-1}}}{2\sigma_{sSFR_i}}, \tag{4}$$

where i is the index of the stellar mass bin and N is the number of galaxies in that bin (Rao 1973). We then combine this in quadrature with the error calculated from 100 bootstrap resamples of the
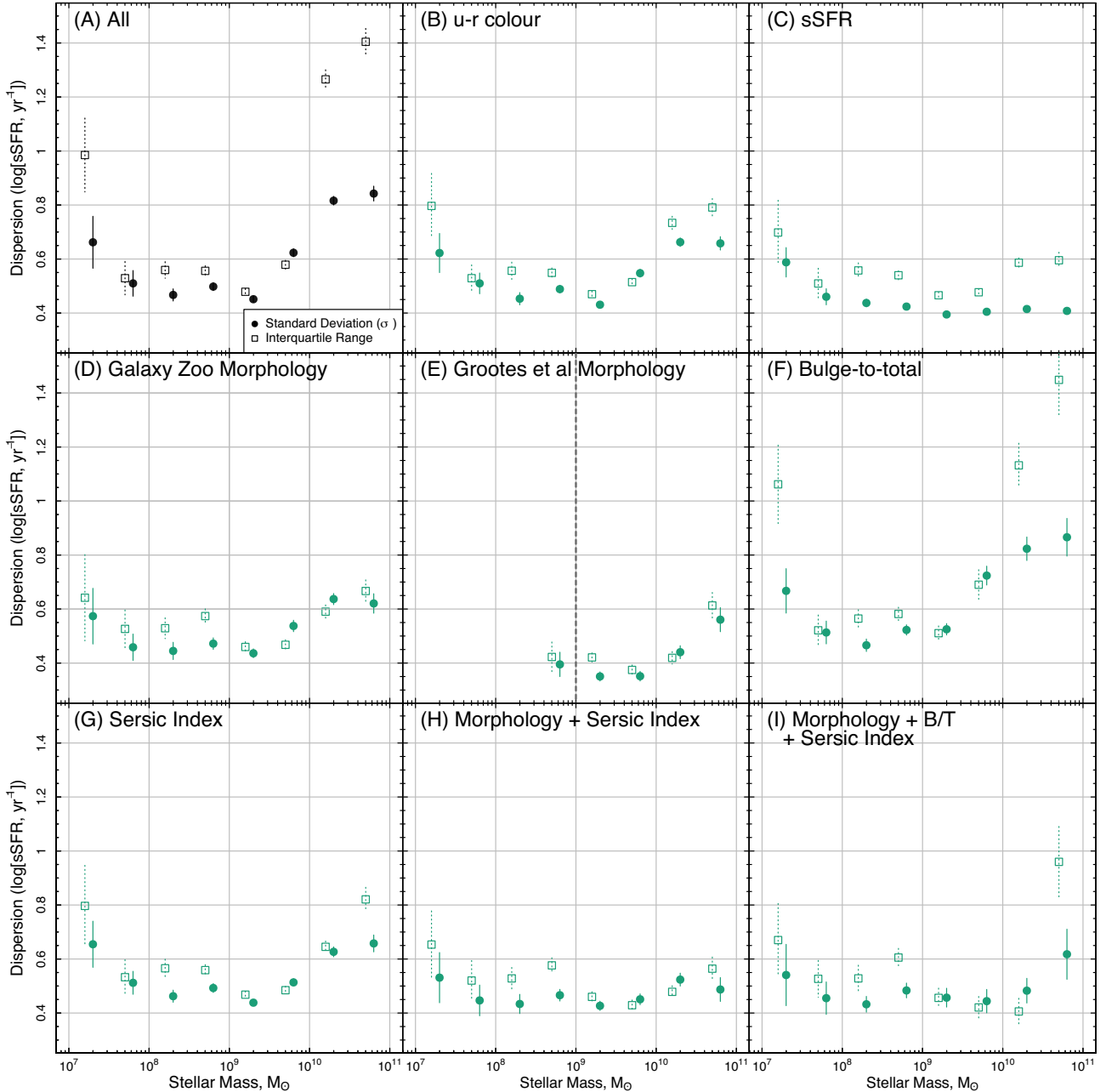
Figure 4. The resultant dispersion along the sSFR–M_* relation measured using both the standard deviation (σ_{sSFR}–M_*, filled circles) and interquartile range (open squares). Each panel shows a different method for isolating the SFS described in Section 3. This Figure follows the same layout as Fig. 2, but only using SFS-selected population (green points when both green and red are present in Fig. 2). While the normalization and shape changes, the majority distributions show a 'U'-shaped dispersion with minimum at $\sim 10^9.25\,\mathrm{M_\odot}$ and increased scatter at low and high masses for both σ_{sSFR} and interquartile range.

population within the errors of both stellar mass and SFR. For errors on the interquartile range, we only apply the bootstrap resampling errors. This bootstrap resampling is intended to take into account the varying measurement error in each of our SFR indicators as a function of stellar mass.

First, we find that the majority of the panels show close to 'U'-shaped distribution with minima at $\sigma_{\mathrm{sSFR}} \sim 0.35$–0.5 dex and $\log_{10}[M_*/\mathrm{M_\odot}] = 8.5$–9.5 (in the following section, we fit these distributions with a second-order polynomial to find the minimum points). We observe a steep increase in both σ_{sSFR} and interquartile range to higher stellar masses than this minima. The increase to

lower stellar masses is much shallower but tentatively observable in both measures of dispersion. These results are roughly consistent with observations of Guo et al. (2015) and Willett et al. (2015) modulo slight differences in normalization ($\sim$0.1 dex) and have comparable scatter to the recent results of Boogaard et al. (2018). We also find a consistency between the dispersion measured using both σ_{sSFR} and the interquartile range at most stellar masses, this indicates that the assumption of a lognormal distribution of sSFRs at a given stellar mass is appropriate. The places where this does not hold true are when stellar masses are either very low or very high (this is also displayed in the larger kurtosis values in Fig. 3).

In these regimes, the interquartile range may be a more accurate representation of the dispersion as it does not assume a lognormal distribution.

We find that while sample selection does affect the normalization of the dispersion at specific stellar masses, we do see consistency between sample selections in terms of the minimum point in both stellar mass and dispersion, and in the overall shape; with all samples displaying a dispersion that rises to low and high stellar masses.

We also find that when selecting on sSFR (panel C) we observe a more linear distribution with decreasing σ_{sSFR} to higher stellar masses. This is as expected as a hard cut in sSFR simply removes the high-dispersion population at high stellar masses (see panel C of Fig. 2). In combination, the panels in Fig. 4 suggest that irrespective of the method for selecting a star-forming/disc-like galaxy population based on colour and morphology, in GAMA we observe a 'U'-shaped σ_{sSFR}–M$_*$ relation, which is largely consistent with the previous observations of Guo et al. (2015) and Willett et al. (2015).

4.0.1 Mixture modelling method

In addition to the physically motivated sample selections described previously, it is also possible to determine the σ_{sSFR}–M$_*$ relation based on mixture modelling of the star-forming and passive population (see Taylor et al. 2015, for a similar approach). Here, we use the [R] MIXTOOLS:NORMALMIXEM function to perform a maximum log-likelihood mixture fit to the two population in $\log_{10}[M_*/M_\odot] = 0.5$ bins of stellar mass at $\log_{10}[M_*/M_\odot] > 8.5$ (below this we assume a single high-sSFR population). The top panel of Fig. 5 shows the sSFR–M$_*$ plane for MAGPHYS-derived SFRs. The green and red lines display the mean (solid lines) and 1σ width (dashed lines) of the mixture models for the high-sSFR and low-sSFR population, respectively.

The bottom panel of Fig. 5 then shows σ_{sSFR}–M$_*$ relation for the high-sSFR population, where errors are calculated using equation (4) but where N is the number of galaxies in a particular stellar mass bin multiplied by the mixing proportion in the high-sSFR population. Once again we find a 'U'-shaped distribution with minima at $\log_{10}[M_*/M_\odot] \sim 9.25$ and σ_{sSFR} increasing to low and high stellar masses. We do find that the normalization of the σ_{sSFR}–M$_*$ relation for our mixtures is slightly lower than for our previous selections (minima at $\sigma_{sSFR} \sim 0.3$ dex), likely due to the fact that large dispersion points are included in the low-sSFR mixture irrespective of their physical properties.

However, it is interesting to highlight that when using non-physically motivated separation between the star-forming and passive population we still observe a 'U'-shaped σ_{sSFR}–M$_*$. This result is therefore once again, unlikely to be driven by choice of sample selection.

4.1 Variation with SFR indicator

We also consider if the results described above hold true for different SFR indicators; as different observables can provide different measures of star formation with varying degrees of scatter (e.g. see Davies et al. 2016). In addition, other explorations into the dispersion along the SFS have used a number of different SFR indicators. As such, we wish to produce a comparison point to these studies from GAMA in the local Universe.

Hence, we reproduce our analysis for all other SFR indicators discussed in Section 2.1.1. Figures identical to Figs 2 and 4 are given in the appendix for UV + TIR, Hα, W3, and u-band SFRs. In the majority of cases, these figures display a largely 'U'-shaped σ_{sSFR}–M$_*$
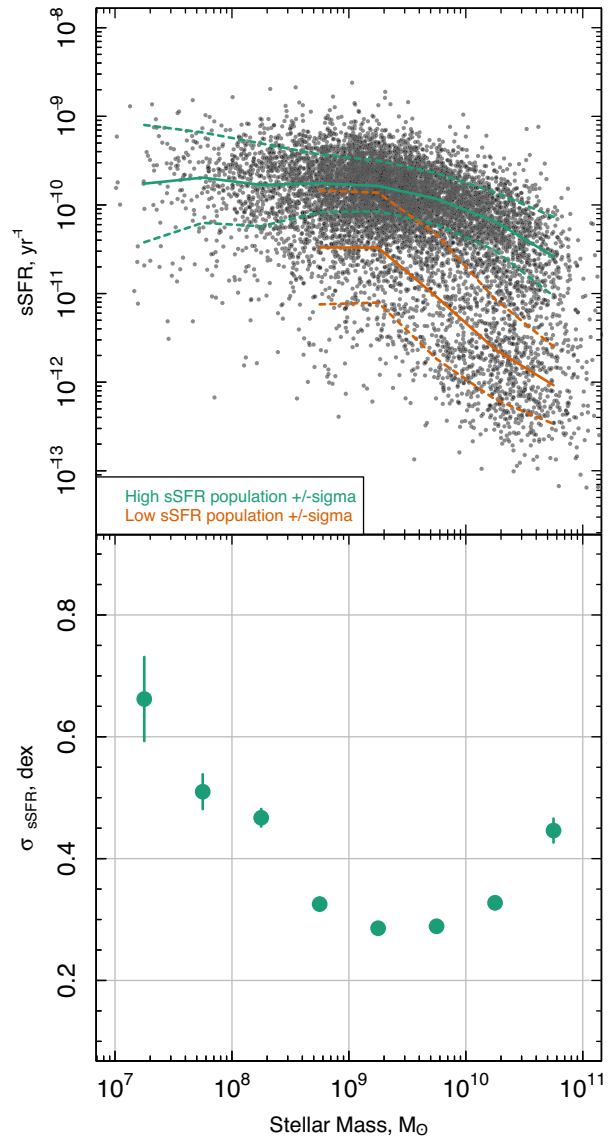

Figure 5. Mixture modelling of the star-forming and passive population assuming lognormal distributions in sSFR. The top panel displays the SFR–M$_*$ plane for MAGPHYS-derived SFRs. The green and red lines display the mean (solid lines) and 1σ width (dashed lines) of the mixture models as a function of stellar mass. The bottom panel shows the σ_{sSFR}–M$_*$ relation for the high-sSFR population.

relation with minimum at $\sigma_{sSFR} \sim 0.35$–0.5 dex and $\log_{10}[M_*/M_\odot]$ = 9–10. They all display a steep increase of dispersion to high stellar masses, and a more tentative, shallow increase to lower stellar masses.

The u-band SFRs (Fig. A4) do have a much smaller dispersion across all stellar masses (minimum at $\sigma_{sSFR} \sim 0.2$–0.3 dex) but retain a 'U'-shape. The changes in normalization of σ_{sSFR} between SFR indicator are likely due to the robustness of each indicator in measuring SFRs and how correlated they are with stellar mass; with high scatter indicative of larger measurement error and/or unknown assumptions in converting from an observable to a true SFR (e.g. see Davies et al. 2016).

In Fig. A5, we produce a comparison of all SFR indicators by scaling the distributions using the minimum dispersion in each indicator. This removes some of the dependence on absolute
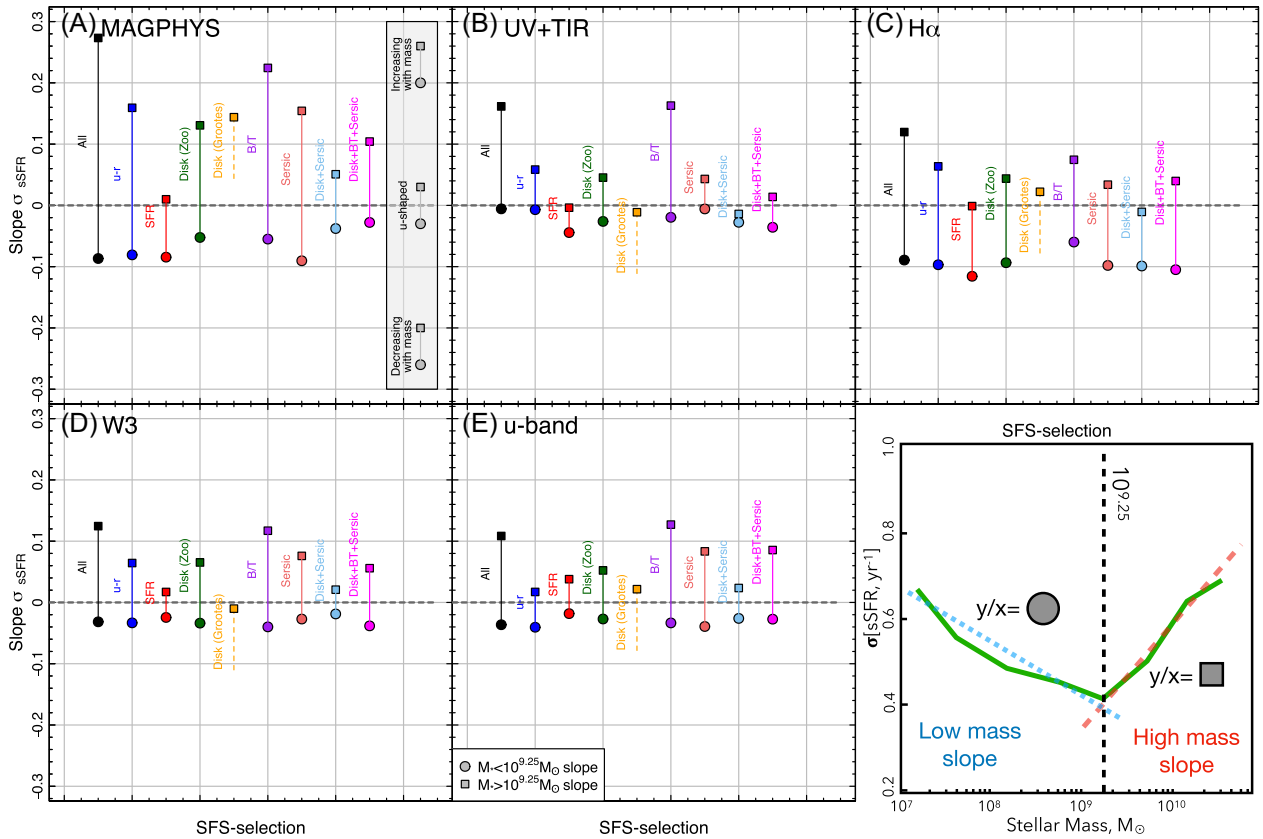
Figure 6. The high-mass and low-mass slope of the $\sigma_{sSFR}-M_*$ relation for different SFR indicators (described in Section 2.1.1) and using each method for isolating the SFS (described in Section 3). We separate the $\sigma_{sSFR}-M_*$ distributions in Fig. A5 and take the high-mass end as $\log_{10}[M_*/M_\odot] > 9.25$ and low-mass end as $\log_{10}[M_*/M_\odot] < 9.25$. We then linearly fit the slope at high (squares) and low masses (circles) – see bottom right-hand panel. Each other panel displays a different SFR indicator, and each pair of points/line displays a different method for isolating the SFS. In this figure, when the pair of points spans the dashed zero line, the distribution $\sigma_{sSFR}-M_*$ is parabolic with a minimum vertex, when they both sit below the dashed zero line σ_{sSFR} decreases with mass, and when they both sit above the dashed zero line σ_{sSFR} increases with mass. The size of the distance between the two points is indicative of how curved the distribution is about $\log_{10}[M_*/M_\odot] = 9.25$. Note that for the Grootes et al. morphological proxy, we only have the high-mass slope. We find that in almost all cases the $\sigma_{sSFR}-M_*$ relation is parabolic (the pairs of points span the dashed zero line). We also note that if we use either $\log_{10}[M_*/M_\odot] = 8.75$ or $\log_{10}[M_*/M_\odot] = 9.75$ as our minimum points it does not significantly alter these results.

normalization between SFR indicators and allows a more direct comparison of their shape. In the majority of cases, each indicator shows a 'U-shape' with largely consistent increases in dispersion to low and high stellar masses, irrespective of SFR used. The most notable exception to this is the UV + TIR indicator. This is largely due to the tfact hat the minimum point in σ_{sSFR} occurs at higher stellar masses for this indicator (close to $\log_{10}[M_*/M_\odot] = 10$).

In order to easily compare the shape of the $\sigma_{sSFR}-M_*$ relation for all SFR indicators and sample selections, we define a simple metric based on the slope of $\sigma_{sSFR}-M_*$ in the low- and high-stellar mass regime; divided at $\log_{10}[M_*/M_\odot] = 9.25$. To choose this reference point, we fit a second-order polynomial to the $\sigma_{sSFR}-M_*$ relation for all samples and SFR indicators and find the median minimum point to be at $\log_{10}[M_*/M_\odot] = 9.261$, hence our closest stellar mass bin is $\log_{10}[M_*/M_\odot] = 9.25$. We then perform a least-squares linear fit to the low-mass and high-mass $\sigma_{sSFR}-M_*$, respectively. This process is described visually in the bottom right-hand panel of Fig. 6. While the point at $\log_{10}[M_*/M_\odot] = 9.25$ does not represent the minimum in all distributions (see above), we wish to use a consistent point across all $\sigma_{sSFR}-M_*$ relations to highlight any variation with sample selection and/or SFR indicator. However, we do repeat this analysis for slopes about both $\log_{10}[M_*/M_\odot]$

$= 8.75$ and $\log_{10}[M_*/M_\odot] = 9.75$ and find consistent results. While this is potentially a crude metric for the shape of the distributions, it allows an easy comparison of multiple different samples in the same figure.

Fig. 6 displays these low- and high-mass slopes for each sample selection (colours) and for each SFR indicator (panels). In this figure, points that span the $y = 0$ line have a 'U'-shaped distribution. In addition, the separation between the points (length of the coloured lines) describes how curved the distribution is, with points close together indicating a linear relation, and far apart a highly curved distribution. For samples that cross the $y = 0$ line, the position where the coloured line crosses the $y = 0$ line describes the asymmetry of the distribution about $\log_{10}[M_*/M_\odot] = 9.25$. For example, a purely symmetric 'U'-shape would have widely vertically spaced points with the dashed $y = 0$ crossing at the mid-point of their connecting line.

From this figure, we see that the majority of our samples have widely separated points that span the $y = 0$ line. This metric displays, at a glance, that irrespective of sample selection or SFR indicator the $\sigma_{sSFR}-M_*$ relation is U'-shaped with minimum close to $\log_{10}[M_*/M_\odot] = 9.25$ and increasing dispersion to low and high stellar masses. The exception to this is the selection using sSFR that
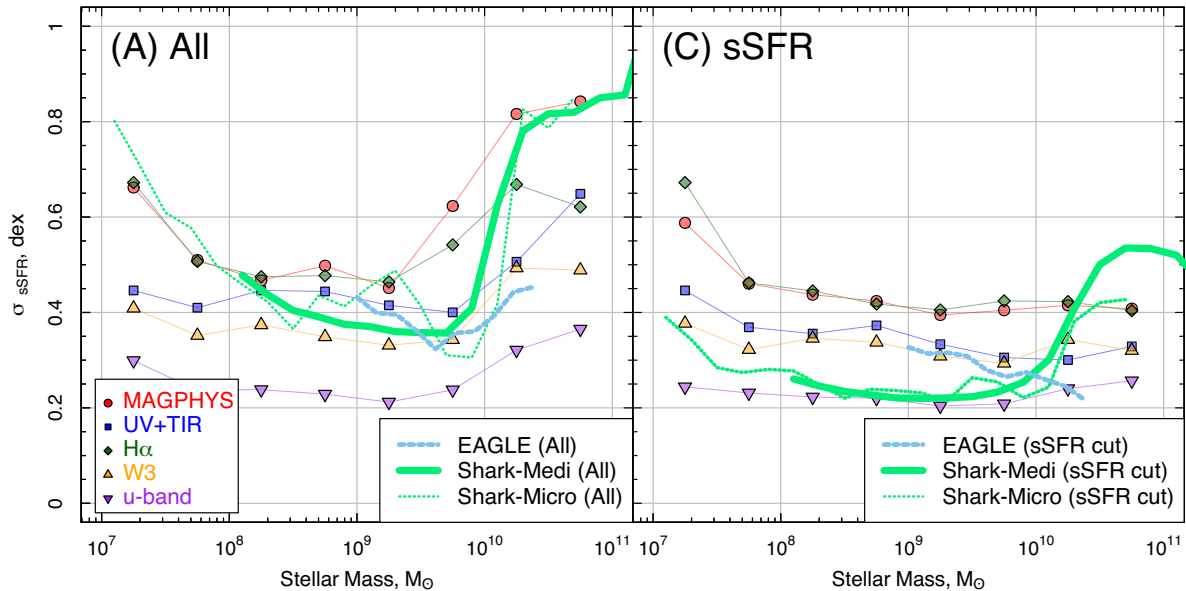
Figure 7. σ_{sSFR}–M_* relation from the Shark SAM (solid green) compared to our observations for different SFR indicators (coloured points) and the EAGLE simulation results (dashed blue lines). The left-hand panel displays the relation for all galaxies, while the right-hand panel shows only galaxies with $\log_{10}[sSFR, yr^{-1}] > -11$. Both simulations are only shown above their mass resolution limits. Shark displays a remarkably similar distribution to our data in the left-hand panel, and both Shark and EAGLE show a similar relation but offset slightly in normalization in the right-hand panel at $\log_{10}[M_*/M_{\odot}] < 10$. At the highest stellar masses, we see an upturn for Shark, which is not found in EAGLE or the observations; due to that fact that in Shark, star formation in very massive galaxies declines slowly and galaxies stay above the sSFR cut.

has a linearly decreasing dispersion with stellar mass in the majority of cases (both points sit below the y = 0 line). Once again this is expected as the cut in sSFR removes the large dispersion population at high stellar masses.

4.2 Comparison to the state-of-the-art semi-analytic model and hydrodynamical simulations

In addition to the Katsianis et al. (in preparation) results from EAGLE discussed previously, we also compare our observed σ_{sSFR}–M_* relation to the state-of-the-art SAM Shark (Lagos et al. 2018). Briefly, Shark is a highly flexible and modular open-source SAM, which includes several different models for gas cooling, AGN, stellar and photoionization feedback, and star formation. Here, we use the Shark parameters described in Lagos et al. (2018) run over the SURFS (Elahi et al. 2018) simulations with Planck15 cosmology and take the Shark + SURFS galaxies in the z = 0 shapshot. We use both the medi-SURFS (medium box size and medium mass resolution) and mirco-SURFS (small box size and high-mass resolution) simulation runs (we do not go into further details of the simulations here, for more details see Elahi et al. 2018 and Lagos et al. 2018). Using the Shark-simulated galaxies, initially we take all isolated central galaxies (as in GAMA) and bin in stellar mass bins of $\log_{10}[M_*/M_{\odot}]$ = 0.2 dex. We then calculate the standard deviation of sSFRs in each bin (consistent with our observational data). For details of the EAGLE results and in-depth discussion of the EAGLE σ_{sSFR}–M_* relation, see Katsianis et al. (in preparation).

The left-hand panel of Fig. 7 displays the σ_{sSFR}–M_* relation using all SFR indicators used in this work for all isolated galaxies overlaid with the relations measured from both Shark and EAGLE (Note that for EAGLE we also only include all isolated central galaxies at z ∼ 0). We find that the σ_{sSFR}–M_* relation from both simulations are consistent with the GAMA results; showing a 'U' shape with minimum at $\log_{10}[M_*/M_{\odot}]$ = 9–10 and a steep rise at higher stellar

masses (albeit only over a small stellar mass range for EAGLE). We also highlight the gradual rise to lower stellar masses in the Shark results, which is observed in some of our SFR indicators. This falls below the mass resolution limit for EAGLE.

We also replicate the sample with a $\log_{10}[sSFR, yr^{-1}] > -11$ cut (right-hand panel of Fig. 7), where both EAGLE and Shark follow a similar relation to the observational data at low to intermediate stellar masses, which sits within the spread of the different SFR indicators explored here. At the highest stellar masses, we still see an upturn in σ_{sSFR} for Shark, which is not found in EAGLE or the observations. This is due to the fact that in Shark, star formation in very massive galaxies declines slowly and galaxies stay above the sSFR cut. In EAGLE, massive galaxies tend to quench rapidly, dropping below the sSFR cut. We also note that the EAGLE mass resolution is limited at $\log_{10}[M_*/M_{\odot}] \sim 9$ and the resolution limit for Shark is $\log_{10}[M_*/M_{\odot}] \sim 8$ for medi-SURFS and $\log_{10}[M_*/M_{\odot}] \sim 7$ for micro-SURFS.

In summary, the Shark model reproduces the observed σ_{sSFR}–M_* relation across all stellar masses incredibly well given that it was not specifically tuned to reproduce the dispersion in this plane, while EAGLE reproduces the relation well above its resolution limit. We note here again that within EAGLE, Katsianis et al. (in preparation) attribute the high dispersion at low and high stellar masses to stellar and AGN feedback, respectively. It is worth highlighting that both EAGLE and Shark use a physical model for AGN and stellar feedback (i.e. not a simple mass scaling that may artificially produce these results). In addition, Lagos et al. (2018) showed that the scatter of the SFS is very sensitive to the adopted star formation law; that is both the way that the interstellar medium is partitioned between ionized, atomic, and molecular gas, and the way molecular gas is converted into stars. Various theoretical and empirical models for star formation were used leading to >0.2 dex differences in σ_{sSFR}. These results suggest that the interplay between gas/stars within the galaxy can also play a significant role in shaping the σ_{sSFR}–M_* relation.
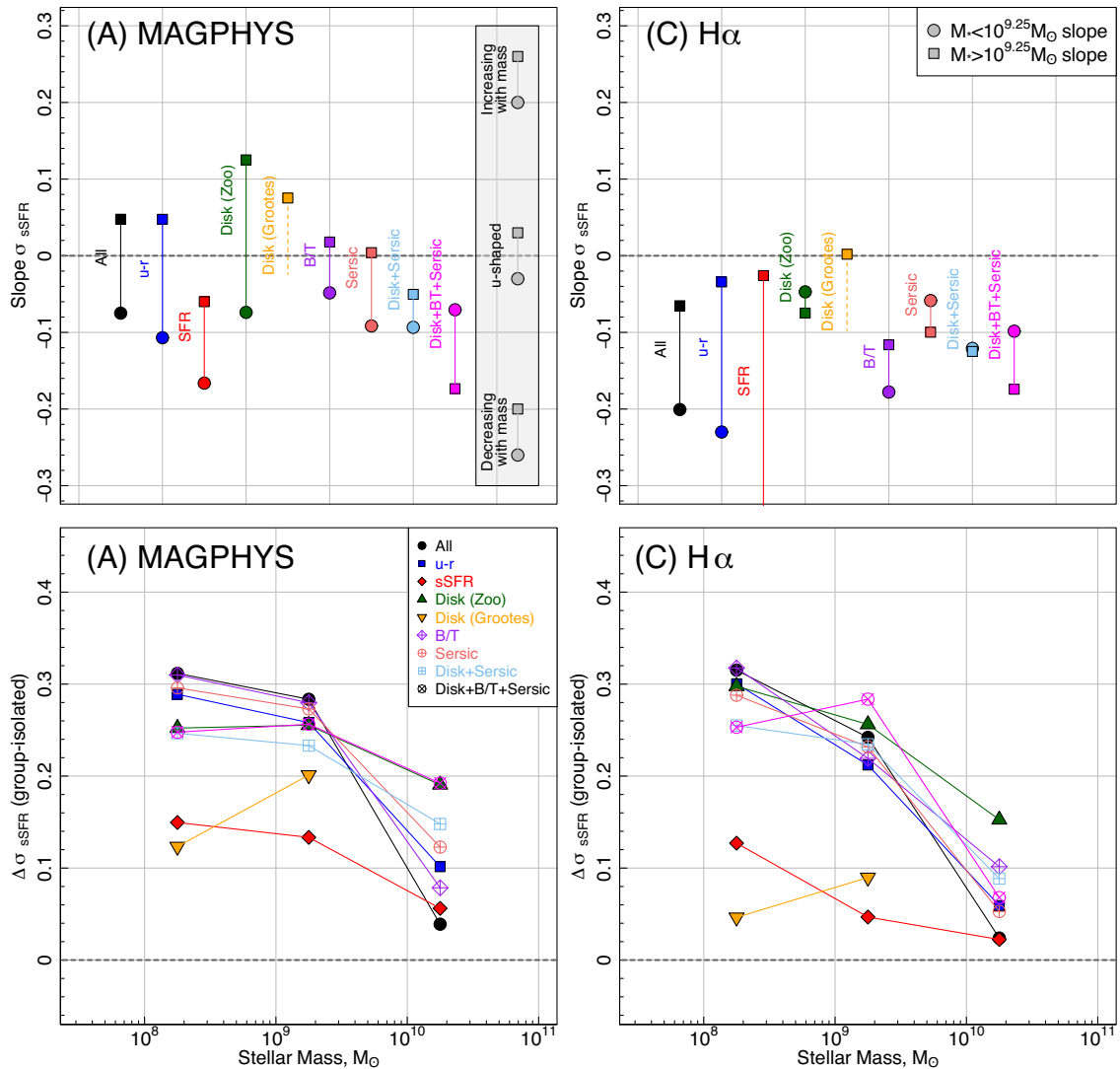
Figure 8. Top: The same diagnostic displayed in Fig. 6 but for just MAGPHYS and H α-derived SFRs in group satellite galaxies. The differences between these panels and Fig. 6 highlight additional sources of scatter in the σ_{sSFR}–M_* relation in groups (see text for details). Bottom: The relative difference between σ_{sSFR} for group satellites and σ_{sSFR} for isolated galaxies in three stellar mass bins. We find increased dispersion in group satellites at all stellar masses ($\Delta\sigma_{sSFR} > 0$), which is more extreme at low and intermediate masses.

4.3 The impact of group environment

Finally, we consider the impact of group-scale environments on the metric used to parametrize the shape of the σ_{sSFR}–M_* relation in Section 4.1. Differences between these metrics for isolated and group environments can potentially elucidate additional physical sources of dispersion in the sSFR–M_* relation caused by group astrophysical processes. To reduce confusion in the number of samples displayed, in this section we will only focus on MAGPHYS and H α-derived SFRs.

To explore the effect of group environment, we select all galaxies within our volume-limited samples that are in an $N > 2$ group from the GAMA group catalogue of Robotham et al. (2011). We then exclude all sources that are closest to the iterative centre of the group as a central. The remaining sources form our 'group satellites' sample, for which we repeat all of the analysis in the previous sections.

The top row of Fig. 8 displays the same metric as in Fig. 6 but for the group satellites. There are two notable differences: (i) the pairs of points for each sample selection are closer together indicating that the distribution is less curved, and (ii) the points are more negative both at the high- (squares) and low- (circles) mass end indicating that in most cases the distributions are no longer 'U' shaped but have a decreasing σ_{sSFR} with increasing stellar mass.

However, the top row of Fig. 8 does not inform as to whether the observed changes are caused by the dispersion increasing or decreasing in group environments, only that the relative shape of the σ_{sSFR}–M_* relation changes. To explore this further, the bottom row of Fig. 8 displays the normalization difference of σ_{sSFR} between the isolated and group satellite samples at three stellar mass bins (i.e. for each independent sample selection and SFR indicator we measure the offset between $\log_{10}[\sigma_{sSFR}]$ in isolated and group environments at $\log_{10}[M_*/M_\odot] = 8.25$, 9.25, and 10.25). We find that σ_{sSFR} is larger in group satellites than in isolated galaxies for all samples
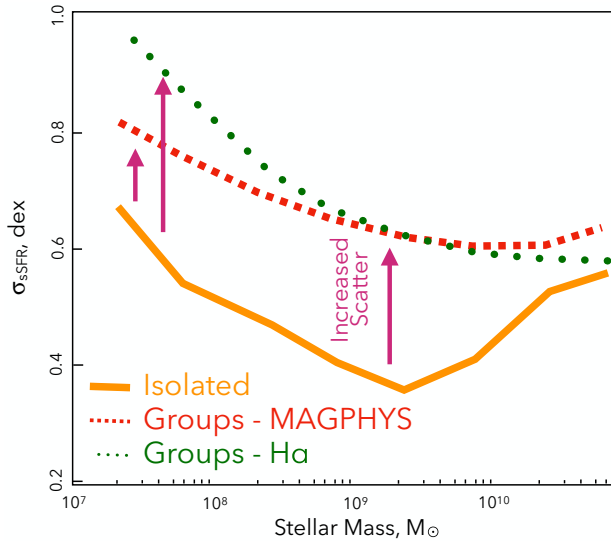
Figure 9. Cartoon representation of the differences in observed σ_{sSFR}–M_* relation between isolated and group environments. The parabolic distribution observed in isolated galaxies is removed by additional large dispersion at low and intermediate stellar masses.

and at all stellar masses (i.e. all points are above zero), but that the increase in dispersion is much larger at low and intermediate stellar masses than at high stellar masses. This indicates that group environments preferentially increase σ_{sSFR} for low-mass galaxies, likely due to increased satellite quenching low-mass galaxies leading to increased dispersion (this is explored in detail in Davies et al., in preparation). To highlight this, Fig. 9 shows a cartoon representation of how the σ_{sSFR}–M_* relation changes between isolated and group satellite galaxies.

To explore the population that is driving the observed differences between isolated galaxies and group satellites further, we return to the full sSFR–M_* plane and compare the distribution of sources in each environment. Fig. 10 displays the H α and MAGPHYS sSFR–M_* plane for isolated galaxies (top rows) and group satellites (bottom row) selected as disc-like systems using the combined Galaxy Zoo morphology and Sérsic index selection. The dashed vertical lines display the points at which we measure the normalization difference in σ_{sSFR} for Fig. 8.

First, we find that there is uniformly larger dispersion along the SFS population at all stellar masses in groups; potentially due to more stochastic star formation processes occurring in groups via interactions. We also find an additional population of quenched group satellite galaxies at $\log_{10}[M_*/M_\odot] \sim 9$–10. To highlight this, in Fig. 10 we colour all galaxies with sSFR$_{H\alpha} < 10^{-11.2}$ in red. This population increases σ_{sSFR} at the point where σ_{sSFR}–M_* is a minimum in isolated galaxies, removing the 'U'-shape shape. This population is likely produced by group-quenching processes (such as strangulation/starvation/stripping). We leave detailed discussion of potential physical mechanisms that may produce these population to the following papers in this series.

However, interestingly we note that this population sits on a tight sequence when using H α-derived SFRs, but is much more dispersed to higher sSFR when using MAGPHYS-derived SFRs. This potentially indicates that group satellites that appear passive in H α-derived SFRs are still transitioning across the green valley when using MAGPHYS-derived SFRs. There are two important differences between SFRs measured using these indicators: (i) GAMA H α

SFRs are derived from fibre-fed spectroscopy and therefore only probe the central regions of galaxies, while MAGPHYS SFRs are integrated over the whole galaxy, and (ii) H α SFRs probe a much shorter integrated physical time-scale than MAGPHYS SFRs (i.e. <20 Myr as compared to <100 Myr, e.g. Davies et al. 2015a). The differences in the red points in different columns of Fig. 10 could be attributed to sources that have quenched on short time-scales, and thus still have residual star formation when measured using MAGPHYS, or sources that are undergoing inside-out quenching and thus become completely passive over the central regions observed by our fibre-fed spectroscopy prior to the whole galaxy becoming passive. We leave detailed discussion of these mechanisms to the following papers, where we aim to produce a more complete picture of the sSFR–M_* plane based on multiple observations.

5 CONCLUSIONS

In the first paper of this series, we have parametrized the dispersion along the SFS for different sample selections and SFR indicators within GAMA. We find that

(i) Irrespective of selection method of star-forming disc-like systems, the σ_{sSFR}–M_* relation is parabolic with high dispersion at the low and high stellar mass end and minimum point of σ_{sSFR} ~ 0.35–0.5 dex at $\log_{10}[M_*/M_\odot] \sim 8.75$–9.75. This holds true for different SFR indicators and when using mixture modelling, albeit with differences in normalization of σ_{sSFR}.

(ii) Our results are largely consistent with a number of previous studies and simulation results from EAGLE, Illustris, and Shark. The EAGLE study suggests that this parabolic dispersion is produced via stellar and AGN feedback at the low- and high-mass end, respectively, while Shark suggests that the interplay between gas/stars within the galaxy can also play a significant role in shaping the dispersion. This will be explored further observationally in subsequent papers in this series.

(iii) In combination, these results suggest that the 'U' shape of σ_{sSFR}–M_* relation is physical and not an artefact of sample selection or method.

(iv) For group satellite galaxies, we find an increased dispersion at all stellar masses potentially due to more stochastic star formation processes occurring in groups. We also find an additional population of quenched sources at $\log_{10}[M_*/M_\odot] \sim 9$–10, which increases σ_{sSFR} and removes the parabolic shape.

(v) We tentatively suggest that this population is produced by group-quenching processes and highlight that differences between H α- and MAGPHYS-derived SFRs for this population may be indicative of short time-scale quenching. However, we leave detailed discussion to the following papers.

We have parametrized the σ_{sSFR}–M_* relation in the local Universe and highlighted that it is a useful tool in exploring the recent SFH of galaxies both in terms of the variation of dispersion as a function of stellar mass and in the differences between isolated galaxies and group satellites. In the following papers in this series, we will explore the morphological evolution across the sSFR–M_* plane and the physical processes that drive the formation of this fundamental relation.
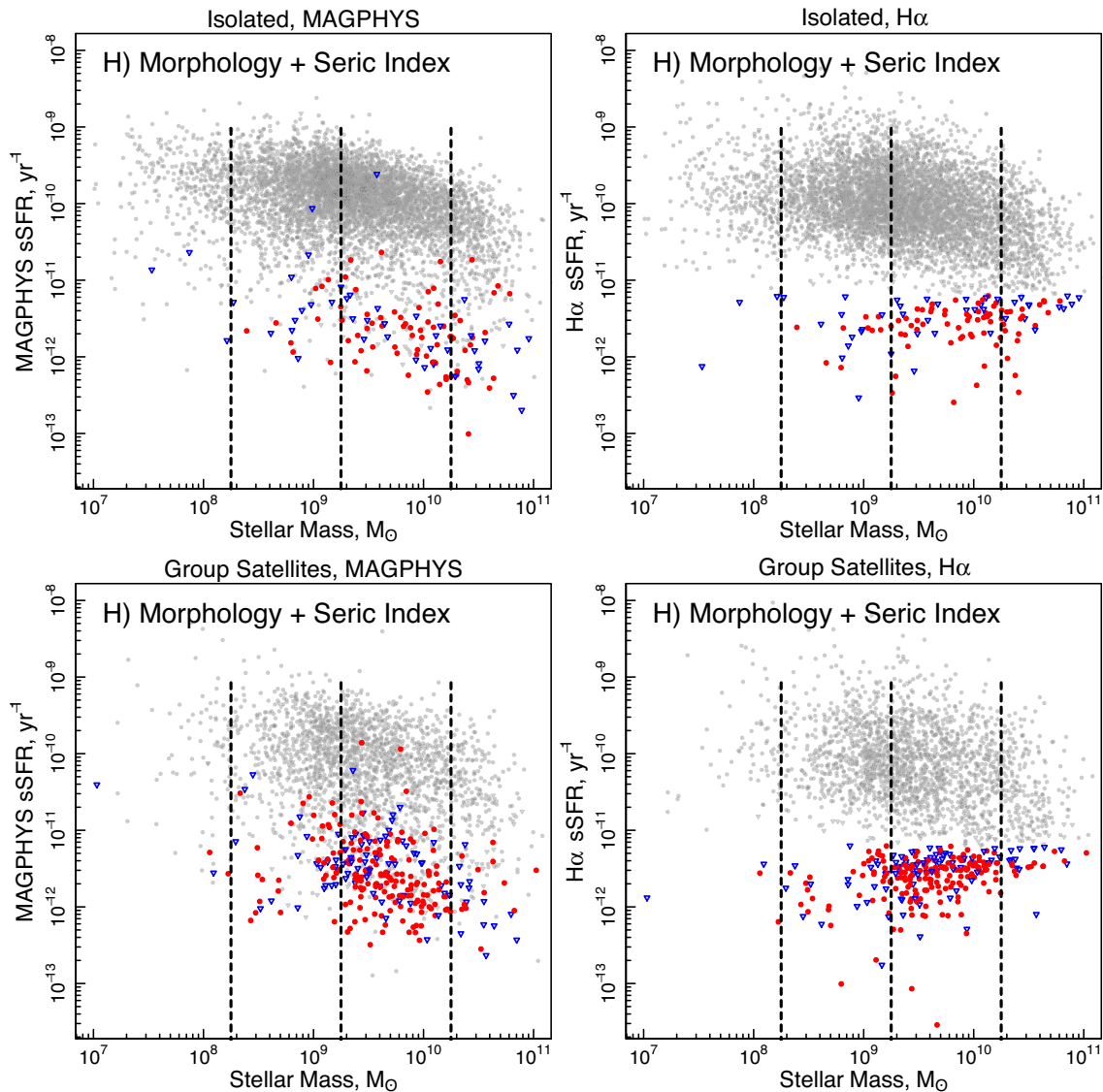
Figure 10. The sSFR–M_* plane for sources selected via Galaxy Zoo morphology and Sérsic index for isolated galaxies (top row) and group satellites (bottom row). Hα and MAGPHYS SFRs are shown in the left-hand and right-hand column, respectively. The dashed vertical lines display the points at which we measure the normalization difference in $\sigma_{\rm sSFR}$ for Fig. 8. The circles display source that have Hα detected at signal-to-noise > 2, while the triangles display sources with Hα signal-to-noise < 2. To highlight the additional quenched groups satellite, population sources with sSFR$_{\rm H\alpha}$ < $10^{11.2}$ are shown in colour (red circles and blue triangles).

GAMA input catalogue is based on data taken from the Sloan Digital Sky Survey and the UKIRT Infrared Deep Sky Survey. Complementary imaging of the GAMA regions is being obtained by a number of independent survey programs including GALEX MIS, VST KiDS, VISTA VIKING, WISE, Herschel-ATLAS, GMRT, and ASKAP providing UV to radio coverage. GAMA is funded by the STFC (UK), the ARC (Australia), the AAO, and the participating institutions. The GAMA website is http://www.gama-survey.org/.

We acknowledge the Virgo Consortium for making their simulation data available. The EAGLE simulations were performed using the DiRAC-2 facility at Durham, managed by the ICC, and the PRACE facility Curie based in France at TGCC, CEA, Bruyeres-le-Chatel.

CL has received funding from a Discovery Early Career Researcher Award (DE150100618) and by the Australian Research Council Centre of Excellence for All Sky Astrophysics in 3 Dimensions (ASTRO 3D), through project number CE170100013.

REFERENCES

Abramson L. E., Gladders M. D., Dressler A., Oemler A., Poggianti B., Vulcani B., 2016, ApJ, 832, 7

Abramson L. E., Kelson D. D., Dressler A., Poggianti B., Gladders M. D., Oemler A., Vulcani B., 2014, ApJ, 785, L36

Baldry I. K. et al., 2010, MNRAS, 404, 86

Baldry I. K. et al., 2018, MNRAS, 474, 3875

Barsanti S. et al., 2018, ApJ, 857, 71

Baugh C. M., 2006, Rep. Prog. Phys., 69, 3101

Boogaard L. A. et al., 2018, A&A, 619, 27

Bouché N. et al., 2010, ApJ, 718, 1001

Bremer M. N. et al., 2018, MNRAS, 476, 12

Brown M. J. I. et al., 2014, ApJS, 212, 18

Bundy K., Fukugita M., Ellis R. S., Kodama T., Conselice C. J., 2004, ApJ, 601, L123

Bundy K., Fukugita M., Ellis R. S., Targett T. A., Belli S., Kodama T., 2009, ApJ, 697, 1369

Chabrier G., 2003, PASP, 115, 763

Cluver M. E., Jarrett T. H., Dale D. A., Smith J. D. T., August T., Brown M. J. I., 2017, ApJ, 850, 68

Conselice C. J., 2014, ARA&A, 52, 291

Cortese L., Catinella B., Boissier S., Boselli A., Heinis S., 2011, MNRAS, 415, 1797

Crain R. A. et al., 2015, MNRAS, 450, 1937

da Cunha E., Charlot S., Elbaz D., 2008, MNRAS, 388, 1595

Daddi E. et al., 2010, ApJ, 713, 686

Dalla Vecchia C., Schaye J., 2008, MNRAS, 387, 1431

Darvish B., Mobasher B., Sobral D., Rettura A., Scoville N., Faisst A., Capak P., 2016, ApJ, 825, 113

Davies L. J. M. et al., 2015a, MNRAS, 447, 1014

Davies L. J. M. et al., 2015b, MNRAS, 452, 616

Davies L. J. M. et al., 2016, MNRAS, 461, 458

Davé R., Katz N., Oppenheimer B. D., Kollmeier J. A., Weinberg D. H., 2013, MNRAS, 434, 2645

de Jong J. T. A. et al., 2013, The Messenger, 154, 44

de Jong J. T. A. et al., 2015, A&A, 582, A62

de Jong J. T. A. et al., 2017, A&A, 604, A134

Dekel A., Silk J., 1986, ApJ, 303, 39

de Ravel L. et al., 2009, A&A, 498, 379

Driver S. P., Davies L. J., Meyer M., Power C., Robotham A. S. G., Baldry I. K., Liske J., Norberg P., 2016b, in Astrophysics and Space Science Proc., Vol. 42, The Universe of Digital Sky Surveys. Springer International Publishing , Switzerland, p. 205

Driver S. P. et al., 2011, MNRAS, 413, 971

Driver S. P. et al., 2016a, MNRAS, 455, 3911

Driver S. P. et al., 2018, MNRAS, 475, 2891

Eales S. et al., 2015, MNRAS, 452, 3489

Elahi P. J., Welker C., Power C., Lagos C. del P., Robotham A. S. G., Cañas R., Poulton R., 2018, MNRAS, 475, 5338

Elbaz D. et al., 2007, A&A, 468, 33

Elbaz D. et al., 2011, A&A, 533, A119

Erfanianfar G. et al., 2016, MNRAS, 455, 2839

Fabian A. C., 2012, ARA&A, 50, 455

Genzel R. et al., 2010, MNRAS, 407, 2091

Giovanelli R., Haynes M. P., 1985, ApJ, 292, 404

Gordon Y. A. et al., 2017, MNRAS, 465, 2671

Grootes M. W., Tuffs R. J., Popescu C. C., Robotham A. S. G., Seibert M., Kelvin L. S., 2014, MNRAS, 437, 3883

Grootes M. W. et al., 2017, AJ, 153, 111

Grootes M. W. et al., 2018, MNRAS, 477, 1015

Gunawardhana M. L. P. et al., 2011, MNRAS, 415, 1647

Gunawardhana M. L. P. et al., 2015, MNRAS, 447, 875

Guo K., Zheng X. Z., Wang T., Fu H., 2015, ApJ, 808, L49

Hill D. T. et al., 2011, MNRAS, 412, 765

Hopkins A. M. et al., 2013, MNRAS, 430, 2047

Jogee S. et al., 2009, ApJ, 697, 1971

Kartaltepe J. S. et al., 2007, ApJS, 172, 320

Katsianis A., Tescari E., Wyithe J. S. B., 2016, Publ. Astron. Soc. Aust., 33, e029

Katsianis A. et al., 2017, MNRAS, 472, 919

Kauffmann G., Heckman T. M., De Lucia G., Brinchmann J., Charlot S., Tremonti C., White S. D. M., Brinkmann J., 2006, MNRAS, 367, 1394

Kauffmann G., White S. D. M., Heckman T. M., Ménard B., Brinchmann J., Charlot S., Tremonti C., Brinkmann J., 2004, MNRAS, 353, 713

Kauffmann G. et al., 2003, MNRAS, 341, 33

Kelvin L. S. et al., 2012, MNRAS, 421, 1007

Kennicutt R. C., Evans N. J., 2012, ARA&A, 50, 531

Lagos C. D. P., Lacey C. G., Baugh C. M., Bower R. G., Benson A. J., 2011, MNRAS, 416, 1566

Lagos C. D. P., Tobar R. J., Robotham A. S. G., Obreschkow D., Mitchell P. D., Power C., Elahi P. J., 2018, MNRAS, 481, 3573

Lange R. et al., 2015, MNRAS, 447, 2603

Lange R. et al., 2016, MNRAS, 462, 1470

Lee N. et al., 2015, ApJ, 801, 80

Lewis I. J. et al., 2002, MNRAS, 333, 279

Lilly S. J., Carollo C. M., Pipino A., Renzini A., Peng Y., 2013, ApJ, 772, 119

Liske J. et al., 2015, MNRAS, 452, 2087

Lotz J. M., Jonsson P., Cox T. J., Croton D., Primack J. R., Somerville R. S., Stewart K., 2011, ApJ, 742, 103

Madau P., Pozzetti L., Dickinson M., 1998, ApJ, 498, 106

Magdis G. E. et al., 2012, ApJ, 758, L9

Matthee J., Schaye J., 2018, preprint (arXiv:1805.05956)

McAlpine S. et al., 2016, Astron. Comput., 15, 72

Mitchell P. D., Lacey C. G., Baugh C. M., Cole S., 2016, MNRAS, 456, 1459

Moore B., Lake G., Quinn T., Stadel J., 1999, MNRAS, 304, 465

Noeske K. G. et al., 2007, ApJ, 660, L43

Oemler A., Jr., Abramson L. E., Gladders M. D., Dressler A., Poggianti B. M., Vulcani B., 2017, ApJ, 844, 45

Peng Y.-jie. et al., 2010, ApJ, 721, 193

Rao C. R., 1973, Linear Statistical Inference and Its Applications, 2nd edn. Wiley, New Yorkp. 625

Renzini A., Peng Y.-jie., 2015, ApJ, 801, L29

Robotham A. et al., 2010, Publ. Astron. Soc. Aust., 27, 76

Robotham A. S. G. et al., 2011, MNRAS, 416, 2640

Robotham A. S. G. et al., 2014, MNRAS, 444, 3986

Rodighiero G. et al., 2010, A&A, 518, L25

Salim S. et al., 2005, ApJ, 619, L39

Salim S. et al., 2007, ApJS, 173, 267

Sancisi R., Fraternali F., Oosterloo T., van der Hulst T., 2008, A&AR, 15, 189

Santini P. et al., 2017, ApJ, 847, 76

Saunders W. et al., 2004, in Moorwood A. F. M., Moorwood I., eds, Proc. SPIE Conf. Ser. Vol. 5492, Ground-based Instrumentation for Astronomy. SPIE, Bellingham, p. 389

Scannapieco C., Tissera P. B., White S. D. M., Springel V., 2008, MNRAS, 389, 1137

Schawinski K. et al., 2014, MNRAS, 440, 889

Schaye J. et al., 2015, MNRAS, 446, 521

Schreiber C. et al., 2015, A&A, 575, A74

Sharp R. et al., 2006, in McLean I. S., Iye M., eds, Proc. SPIE Conf. Ser. Vol. 6269, Ground-based and Airborne Instrumentation for Astronomy. SPIE, Bellingham, p. 62690G

Sparre M. et al., 2015, MNRAS, 447, 3548

Tacchella S., Dekel A., Carollo C. M., Ceverino D., DeGraf C., Lapiner S., Mandelker N., Primack Joel R., 2016, MNRAS, 457, 2790

Taylor E. N. et al., 2011, MNRAS, 418, 1587

Taylor E. N. et al., 2015, MNRAS, 446, 2144

Vogelsberger M. et al., 2014, MNRAS, 444, 1518

Wang E. et al., 2018, ApJ, 860, 102

Whitaker K. E., van Dokkum P. G., Brammer G., Franx M., 2012, ApJ, 754, L29

Willett K. W. et al., 2013, MNRAS, 435, 2835

Willett K. W. et al., 2015, MNRAS, 449, 820

Wright A. H. et al., 2016, MNRAS, 460, 765

APPENDIX A: OTHER SFR INDICATORS

This appendix displays identical figures to Figs 2 and 4 but for all other SFR indicators discussed in Section 2.1.1. Summaries of these figures are displayed in Fig. A5. This figure displays the relation for all indicators, scaled to the $\log_{10}[M_*/M_\odot] = 9.25$ stellar mass bin. To choose this reference point, we fit a second-order polynomial to the σ_{sSFR}–M_* relation for all samples and SFR indicators and find the median minimum point to be at $\log_{10}[M_*/M_\odot] = 9.261$, hence our closest stellar mass bin is $\log_{10}[M_*/M_\odot] = 9.25$. Here, we can more clearly see that in almost all cases the σ_{sSFR}–M_* relation follows a 'U'-shaped distribution. We do find that the stellar mass of the minimum point varies in some cases.
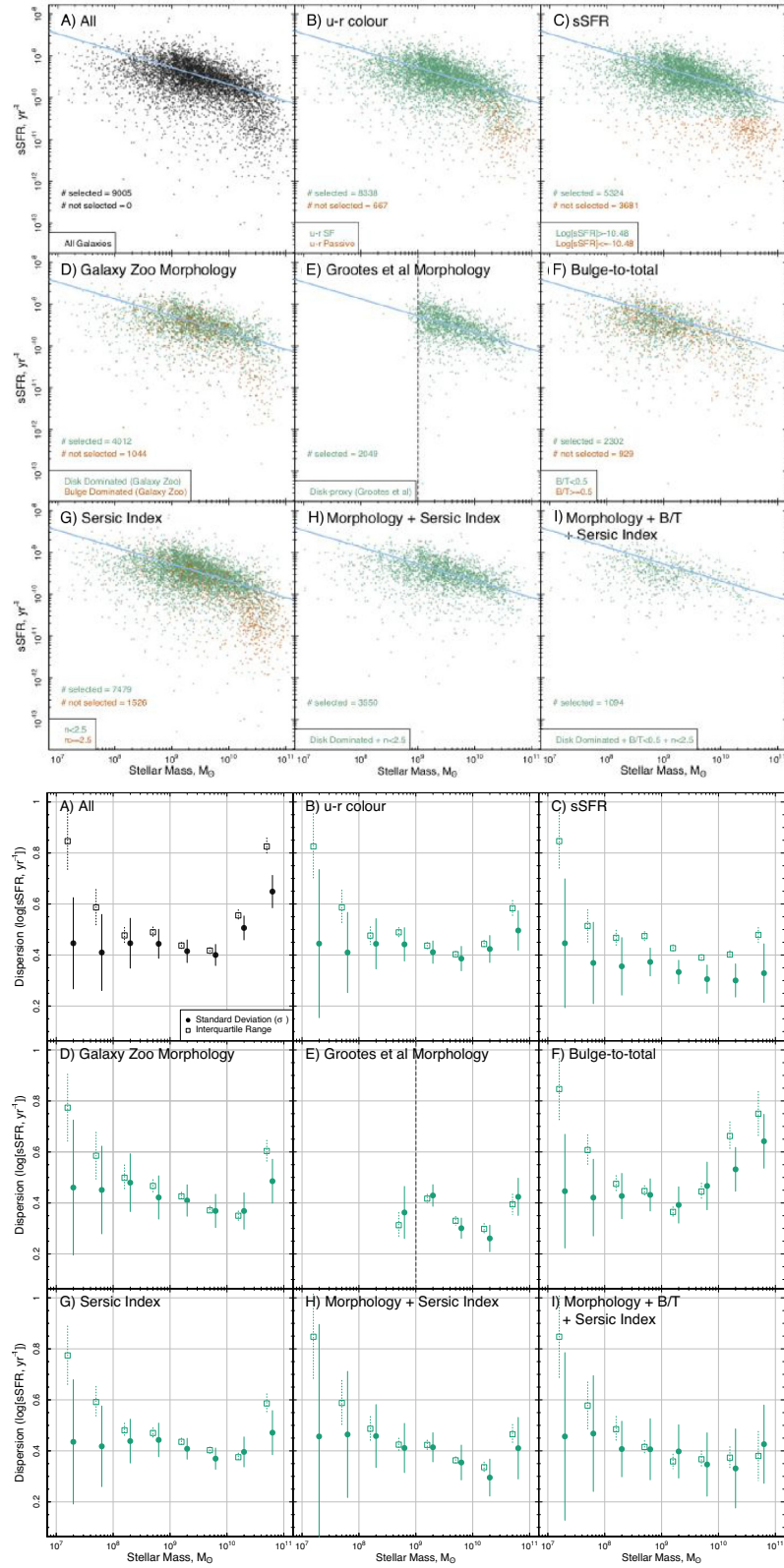
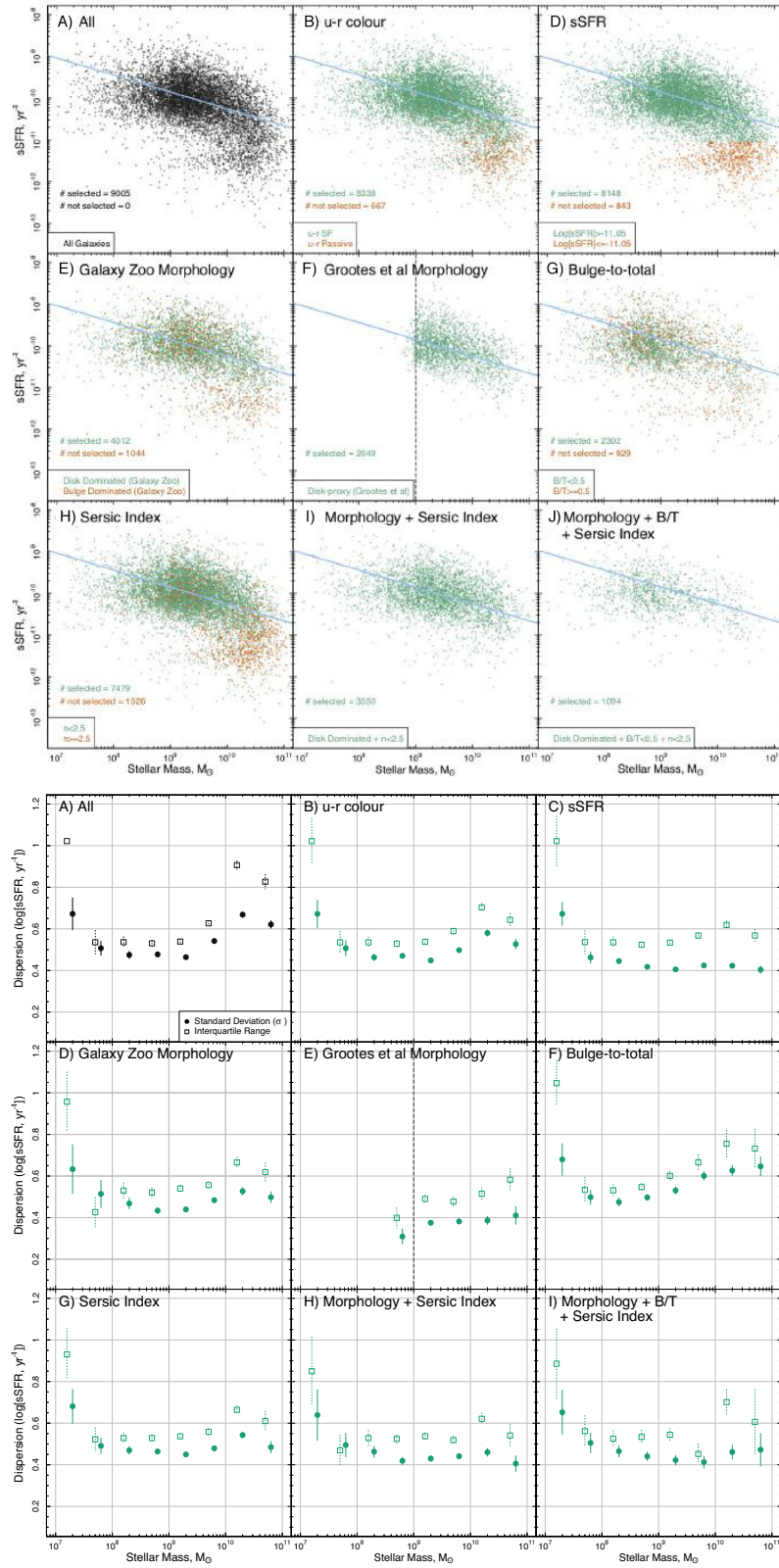**Figure A1.** Same as Figs 3 and 5 but for UV + TIR-derived SFRs.

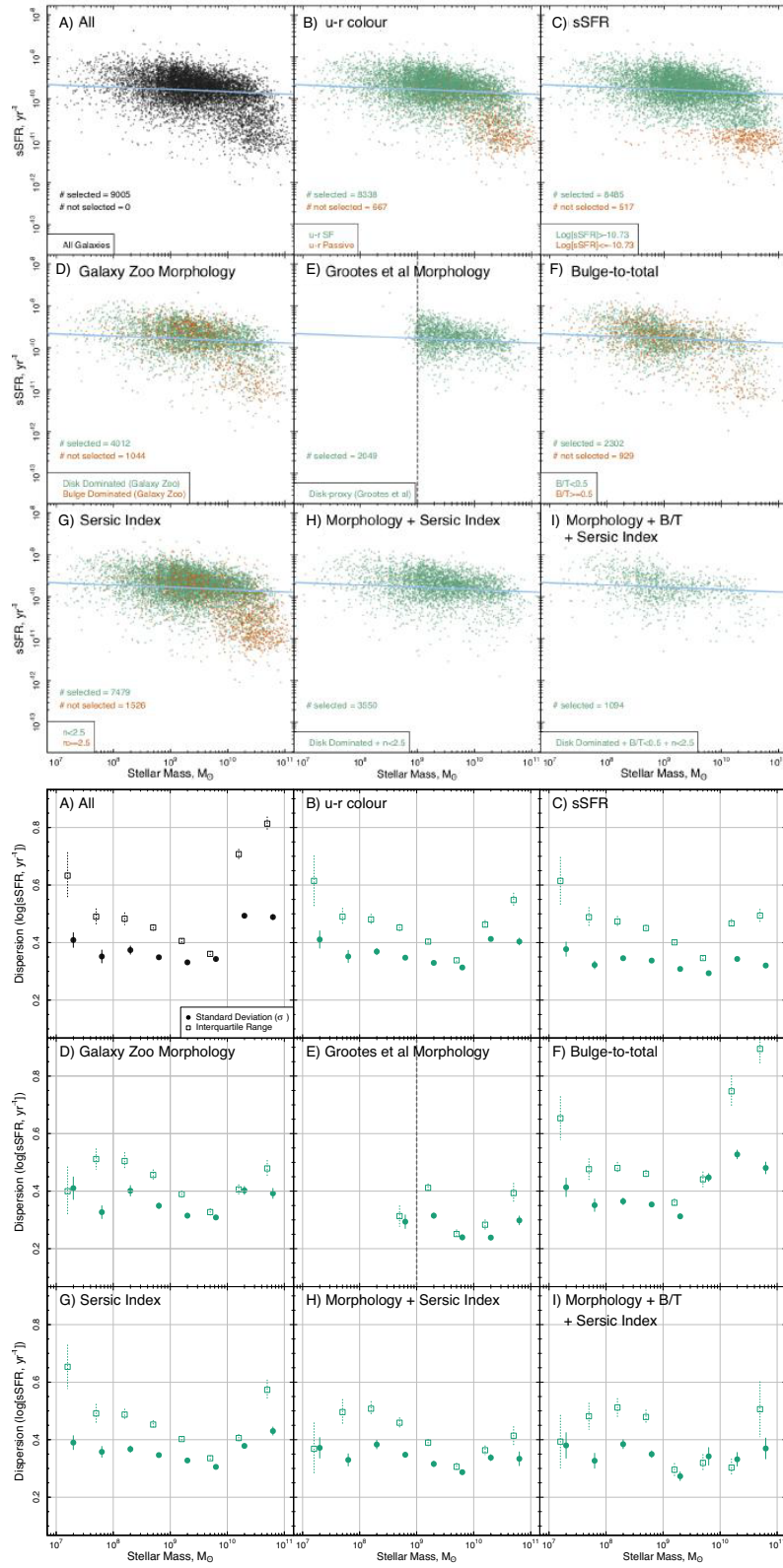**Figure A2.** Same as Figs 3 and 5 but for H α-derived SFRs.

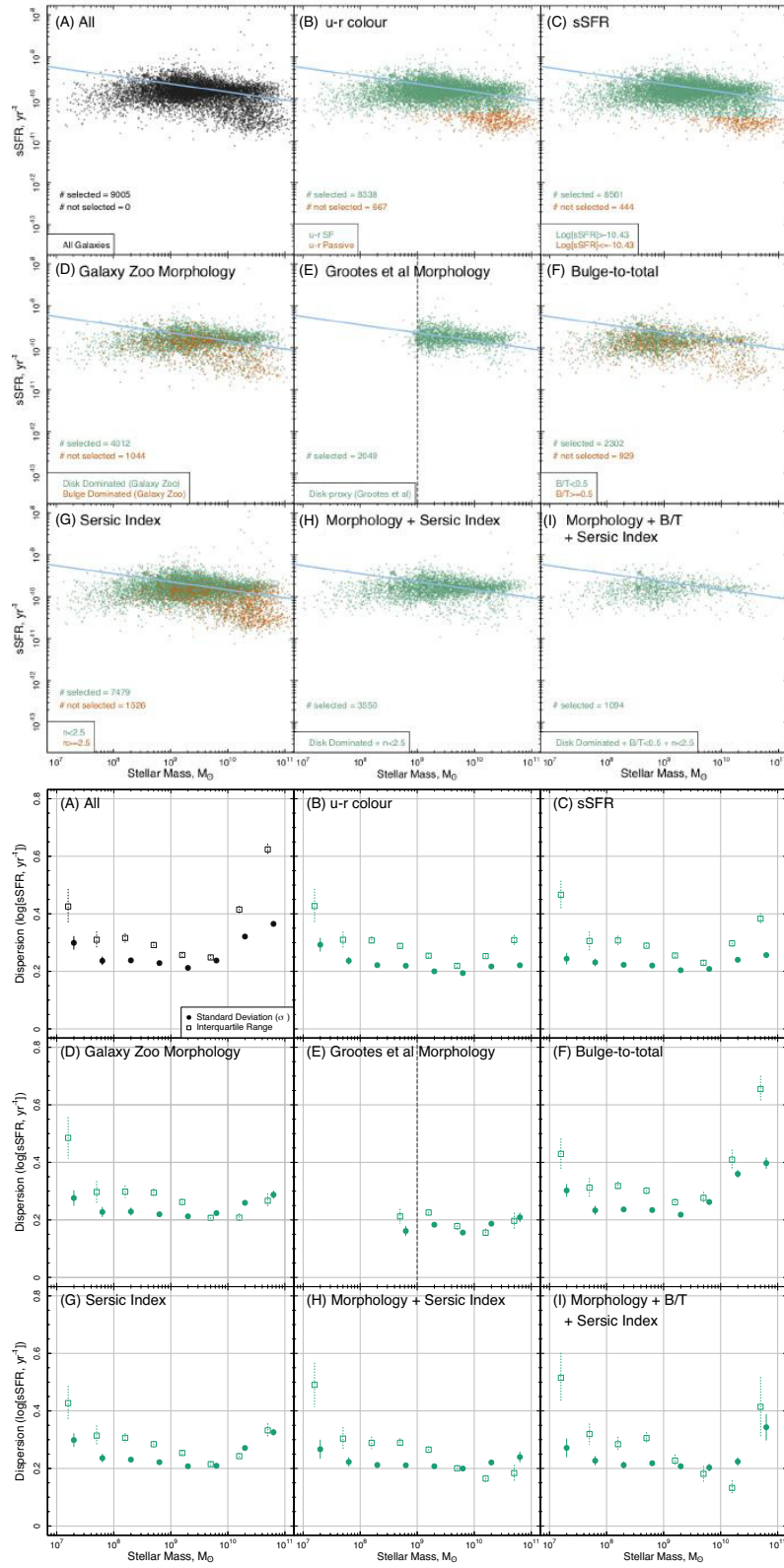**Figure A3.** Same as Figs 3 and 5 but for W3-derived SFRs.

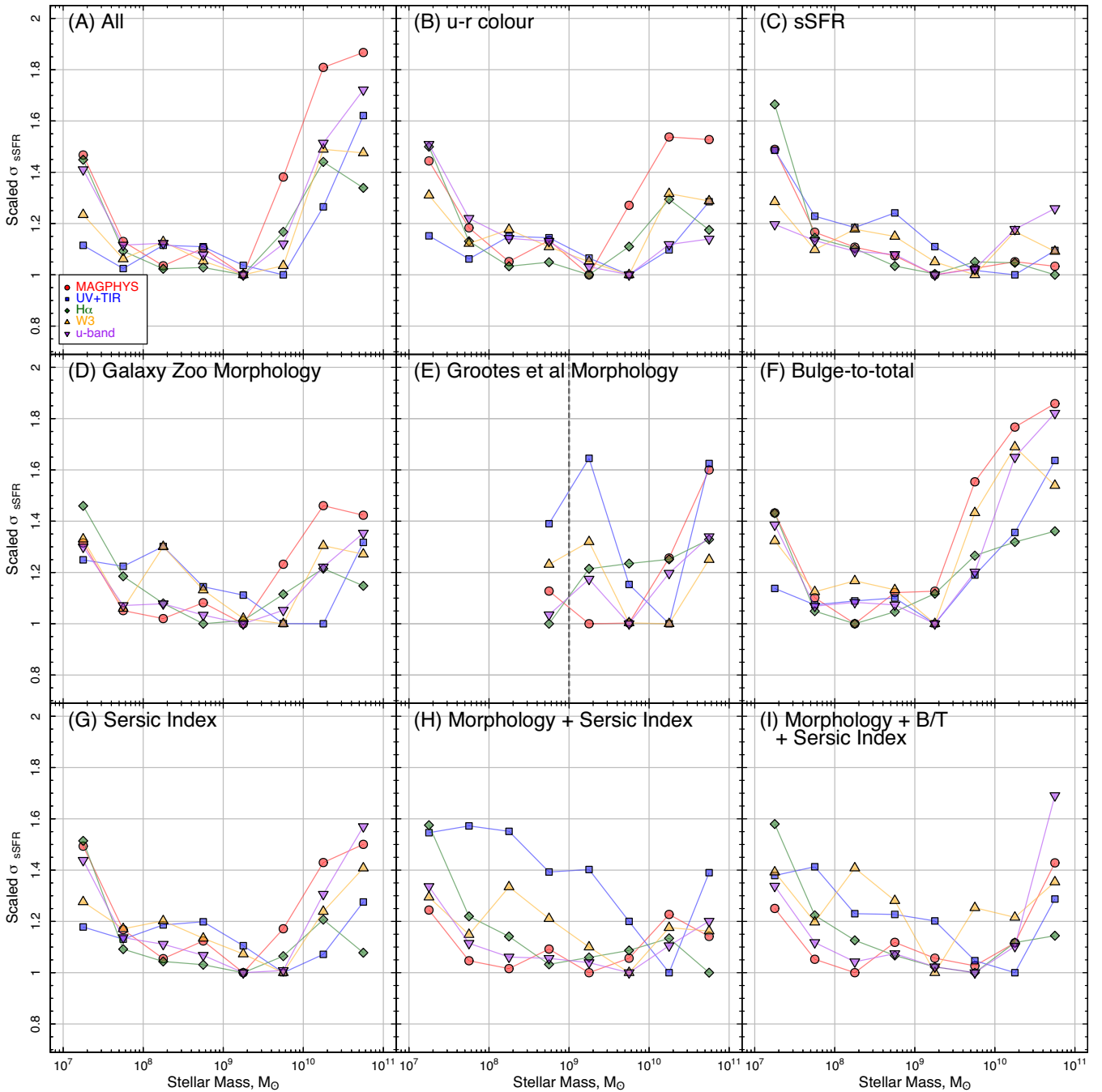**Figure A4.** Same as Figs 3 and 5 but for *u*-band-derived SFRs.

Figure A5. The σ_{sSFR}–M_* relation for different SFR indicators and using each method for isolating the SFS. Figure follows the same layout as Fig. 4, but shows all SFR indicators in each panel – individual SFR indicator figures are given in the appendix. All distributions are scaled, dividing each line by the minimum dispersion for the given SFR indicator. This is intended to remove any dependence on the absolute value of the dispersion and to highlight variations in shape. The majority of the distributions show a 'U-shaped' σ_{sSFR}–M_* relation with minimum at $\sim 10^{9.25}$ M$_\odot$ and increased scatter at low and high masses.

This paper has been typeset from a T$_{\rm E}$X/L$^{\rm A}$T$_{\rm E}$X file prepared by the author.